Structural analysis of protein complexes by cryo electron microscopy

Athanasios Ignatiou[1], **Kévin Macé**[1], **Adam Redzej**[1], **Tiago R. D. Costa**[2], **Gabriel Waksman**[1], **Elena V. Orlova**[1 *]

[1]Institute for Structural and Molecular Biology, School of Biological Sciences, Birkbeck College, London WC1E 7HX, UK

[2] Centre for Bacterial Resistance Biology, Department of Life Sciences, Imperial College London, London SW7 2AZ, UK

*Corresponding author: e.orlova@bbk.ac.uk.

Summary

Structural studies of bio-complexes using single particle cryo-Electron Microscopy (cryo-EM) is nowadays a well-established technique in structural biology and has become competitive with X-ray crystallography. Development of digital registration systems for electron microscopy images and algorithms for the fast and efficient processing of the recorded images and their following analysis has facilitated the determination of structures at near-atomic resolution. The latest advances in EM have enabled the determination of protein complex structures at 1.4-3 Å resolution for an extremely broad range of sizes (from ~100 kDa up to hundreds of MDa [1-7]). In 2022 nearly 12 hundred structures deposited to the EMDB data base were at a resolution of better than 3 Å [7].

To date, the highest resolutions have been achieved for apoferritin which comprises a homo-oligomer of high point group symmetry (O432) and has rigid organisation together with high stability [5,6]. It has been used as a test object for the assessments of modern cryo-microscopes and processing methods during the last five years. In contrast to apoferritin bacterial secretion systems are typical examples of multi protein complexes exhibiting high flexibility owing to their functions relating to the transportation of small molecules, proteins and DNA into the extracellular space or target cells. This makes their structural characterisation extremely challenging [8,9]. The most feasible approach to reveal their spatial organisation and functional modification is cryo-EM. During the last decade structural cryo-EM has become broadly used for the analysis of the bio-complexes that comprise multiple components and are not amenable to crystallisation [10-12].

In this review we will describe the basics of sample preparation for cryo-EM, the principles of digital data collection, and the logistics of image analysis focusing on the common steps required for reconstructions of both small and large biological complexes together with refinement of their structures to nearly atomic resolution. The workflow of processing will be illustrated by examples of EM analysis of Type IV Secretion System.

Keywords:

Cryo-electron microscopy, Sample preparation, Single particle analysis, Image processing, Type IV secretion system

1. Structural studies by cryo-EM of macro-complexes as illustrated by studies of Type IV Secretion Systems

Different approaches have been used to decipher conformational changes linked to the functional activity of complexes. X-ray crystallography, NMR, and Electron microscopy (EM) combined with biochemical and biophysical methods allow deeper understanding of the mechanisms that underlie macromolecular complex functions. This was clearly demonstrated by studies of the ribosome [13-15]. Recent advances in EM such as the invention of direct electron detection cameras, development of automated data collection software, as well as progress in image processing algorithms have dramatically expanded the range of biological macromolecules amenable to studies by structural cryo Electron Microscopy (cryo-EM).

The main advantage of EM is that it does not require the crystallisation of samples and can be used to determine the structures of bio-complexes within a large range of sizes: from ~100 kDa to many MDa. It was found that current cryo-EM methods are the most efficient approaches for analysis of membrane proteins/complexes, and, as for example, for Type IV Secretion Systems (T4SSs). During the last decade image processing methods have been extensively improved allowing the analysis of image quality more consistently and the assessment of distortions caused by the microscope that prevent the determination of high-resolution structures. New approaches have been developed to reveal sample quality more consistently such as its homogeneity, stability, and to differentiate distinct conformations by enabling determination of the distributions of particles within these different states leading to their eventual characterisation [11,16-19]. A few different packages with state-of-the-art image processing algorithms are now routinely used for the analysis of macromolecular complexes exhibiting a range of symmetries, or asymmetry such as EMAN2, RELION, CryoSPARC, Ximdisp, CryoDRGN, and others [16-24].

Another important factor that has contributed to modern achievements is the increase in computing power making it possible to collect tens of thousands of micrographs and analyse millions of particle images from heterogeneous samples [16-24]. Nonetheless, the basic workflow (Figure 1) of sample imaging and image processing remains almost unchanged while computational tools derived from algorithms implemented in new software packages have been radically improved.

The remarkable success in improving the resolution of EM structures during the last decade would not be possible without advances in sample preparation and data collection at

cryogenic temperatures in what we now refer to as “cryo-EM”. This approach for sample preparation and the amalgamation of methods used in X-ray crystallography and EM image processing have made it possible to achieve details at near atomic resolution for many protein complexes (1-9). This has led to the determination of structures in which the main components of Gram-negative bacterial secretion systems have been resolved at the levels approaching the atomic resolution (25-29). The most recent structures of bacterial secretion systems have provided important information regarding the mechanistic details of how bacteria assemble these highly specialised nano-machines to secrete proteins and DNA to the bacterial extracellular space, and to the eukaryotic or bacterial target cells. Among the Gram-negative bacterial secretion systems, Type IV Secretion Systems (T4SSs) possess the unique ability to secrete proteins, DNA or protein-DNA complexes in an ATP-dependent process. The ability of T4SSs to secrete a variety of substrates involved in pathogenesis and the spreading of conjugative plasmids encoding antibiotic resistance genes made this secretion system an important target for structural biology studies. Recently a new structure of the T4SS has been published in Nature at a resolution of 3.5-6 angstrom revealing new features of the nearly complete complex [28].

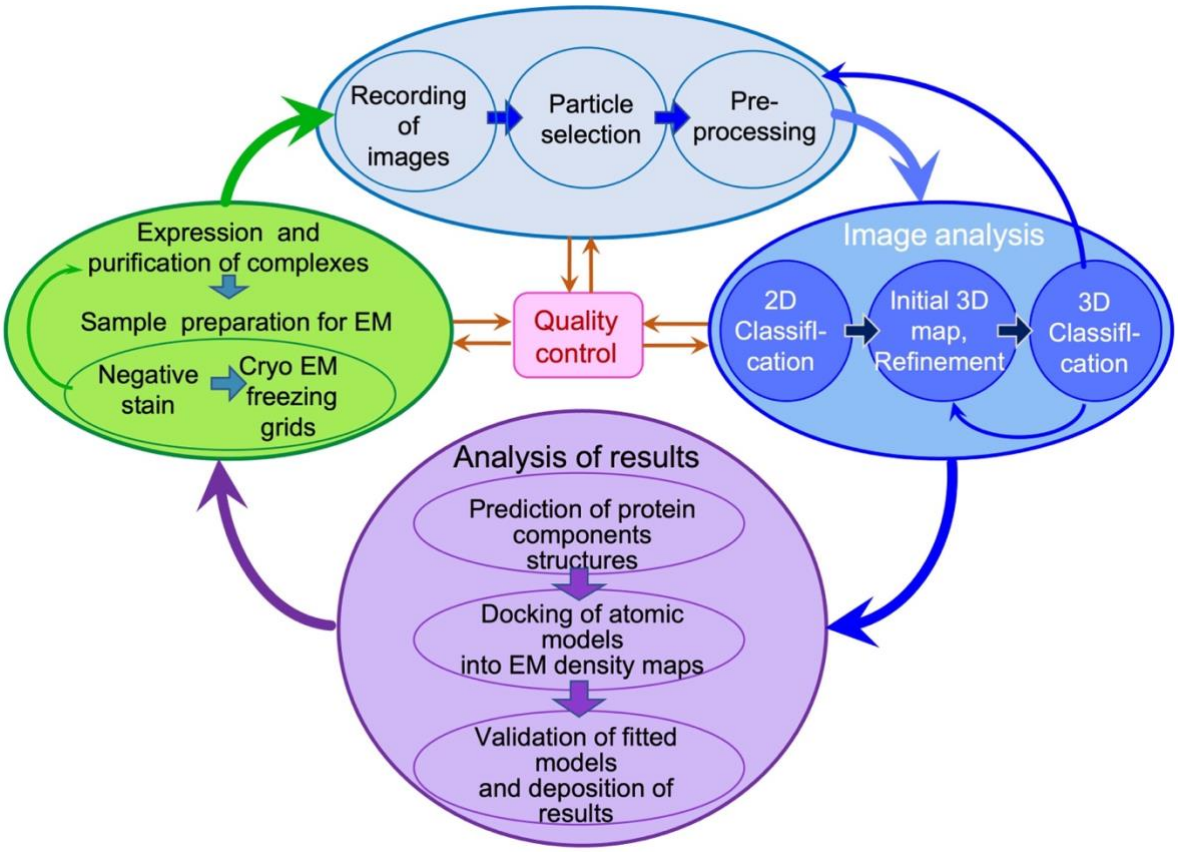

Figure 1. Workflow of EM structural analysis. The biochemical components are highlighted in green while the computational elements are shown in light, dark blue, and purple. The initial steps of processing are shown in light blue which include image frame alignment, CTF estimation and correction, normalisation, and filtering of images. The subsequent steps of alignment, statistical analysis, determination of particle orientations, three-dimensional reconstructions (3D), are shown in dark blue. The final steps (in purple) are related to the interpretation and validation of the reconstructions obtained.

Among all Gram-negative T4SSs, the ones encoded by the Ti plasmid of *Agrobacterium tumefaciens* together with the conjugative pR388, pKM101 and F-plasmids from *E.coli* are the best characterized. These macromolecular complexes comprise at least 11 proteins: from VirB2 to VirB11, and VirD4 [29]. The first main advance in the understanding of the general architecture of a T4SS took place when the cryo-EM structure of the so-called outer membrane core complex (OMCC), encoded by the conjugative pKM101 plasmid, was solved to a resolution of 15Å. This 1.1 MDa structure anchored to the outer membrane is composed of 14 copies of VirB7, VirB9 and VirB10 (Figure 2A) [27]. The OMCC has been obtained at the higher resolution of 12.4Å later and has provided further details of the structural organization of the proteins that form this complex (Figure 2B) [26]. A more complete assembly of the T4SS (VirB3-VirB10) encoded by the conjugative R388 plasmid has been solved by NS (negative staining) EM [27]. This remarkable structure provided the first view of both the OMCC and bipartite inner-membrane complex (IMC) and how these are linked by a structure referred to as the stalk (Figure 2C) [27]. Recently a new structure of the T4SS has been determined at a resolution of 3.5-6 angstrom revealing new features of the nearly complete T4SS complex (Figure 2D) [28].

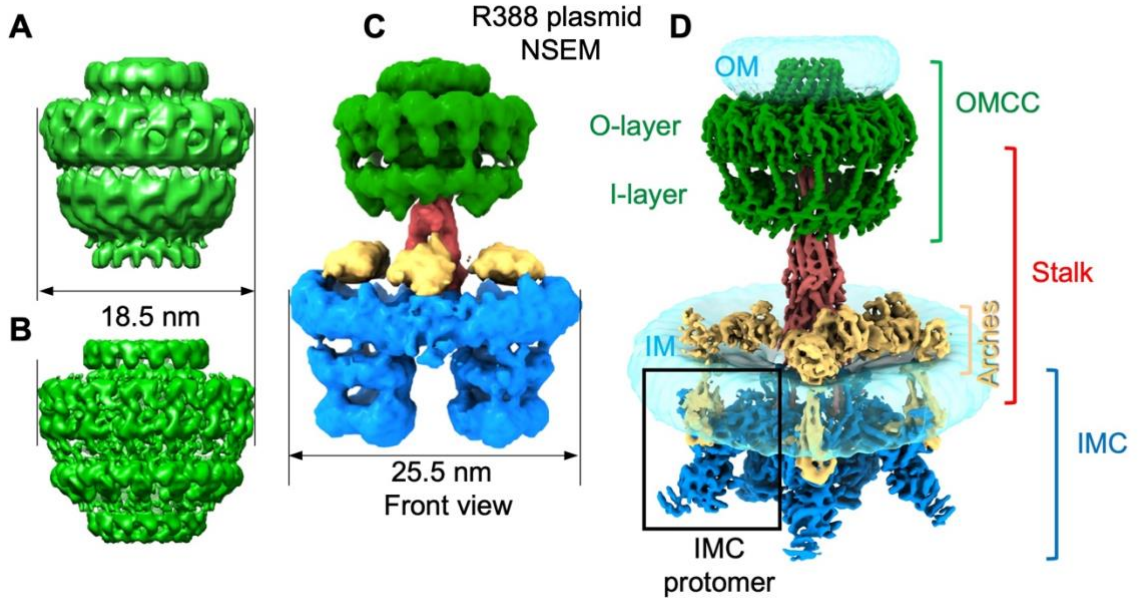

Figure 2. Cryo-EM structures of different T4SS complexes. A. Cryo-EM structure of the outer-membrane core complex (OMCC) at a resolution of 15Å [EMD-5031, 25]. **B.** Cryo-EM structure of the core complex at a resolution of 12.4Å [EMD-2232, 26]. **C.** Structure of the near complete T4SS complex (in negative stain) at overall resolution of ~ 23Å [EMD-2567, Figure adapted from Ref. 27) **D.** Composite electron density map of the R388 T4S system. This map is composed of the assembly of two not symmetrised maps of the OMCC and the IMC at a resolution of 3.3Å and 4 Å respectively, arches and stalk at a resolution of 6.2Å [28]. The OMCC, the stalk, the arches and the IMC are shown in green, red-brown, yellow, and dark blue, respectively [EMD-13765, EMD-13767, Figure adapted from Ref. 28]

From the point of view of a specialist in cryo-EM single particle analysis (SPA), this review may not be considered complete and does not provide sufficient mathematical background for the experienced reader. However, the aim is to provide a general overview of imaging using an electron microscope and the current basic steps of SPA. It will therefore include a brief outline of sample preparation for cryo-EM, the effects of radiation damages, and advances in the procedure for data collection. We describe steps considered as pre-processing and methods used to obtain structures and methods for their validation. More information can be found in other reviews and book chapters [12, 30-32]; should the reader require more details on the subjects described here.

2. Sample preparation in Cryo-EM

While EM provides superior resolution to light microscopy, a more complex procedure for sample preparation has to be employed since samples need to be imaged in a vacuum. This is because images are created by an accelerated beam of electrons within the electron microscope. Under normal circumstances, electrons collide with the atoms that constitute air losing both their energy and scattering directions. To obtain a high-quality image of the sample it is therefore necessary to keep the electron path free of air molecules (i.e., under vacuum) to eliminate unwanted scattering thus enabling them to move directly to the sample. Biological objects (macromolecules and cells) in their native conditions are in aqueous solutions, they therefore have to be made rigid and stable in the microscope column under vacuum to avoid evaporation or changes during the time they are exposed to the electron beam. This requires the use of specialised preparation methods where the dehydration of the sample and staining will minimize molecular distortions or alternatively, stabilization using solidified (frozen) hydrated biological samples [30,33].

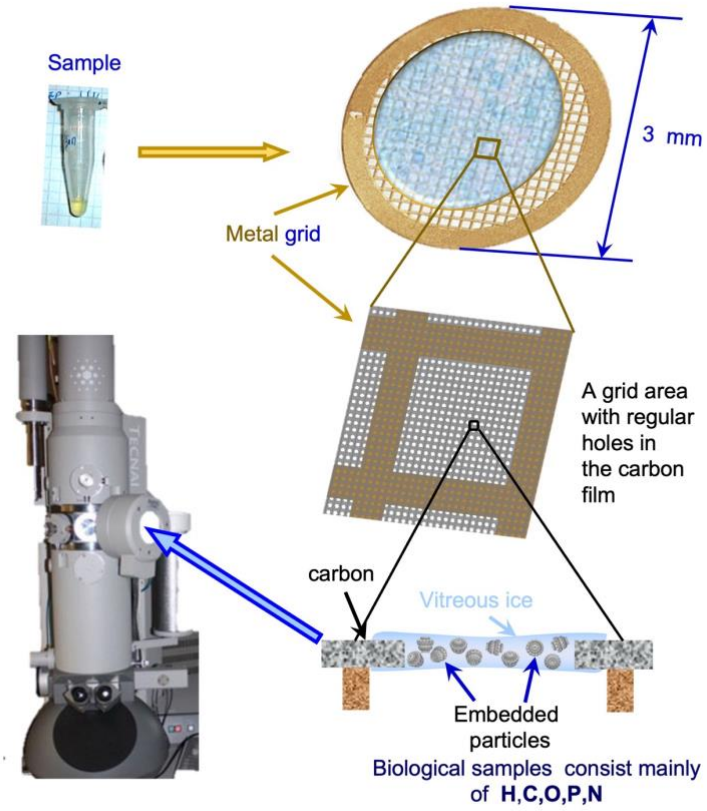

Figure 3. Cryo-EM sample preparation. A. 3 μL of sample is applied to a grid covered with a holey carbon film. **B**. Zoomed in view of a small grid area showing the microscopic holes in carbon film. **C.** Cross-section of a hole with sample particles embedded in vitreous water. **D.** The grid is transferred into a microscope at liquid nitrogen temperature.

Cryo-EM methods of sample preparation allow preservation of the structural integrity of bio complexes keeping them in a nearly native hydrated state in the microscope vacuum. The method proposed by Dubochet, Glaeser and co-workers [33-36] is now used as a well-established technique for freezing aqueous solutions of samples on cryo-EM grids. The EM grid constitutes a round metallic plate (~3mm in diameter and usually made from copper (they can be made from gold, or tungsten) with a fine mesh (typically are used the grids with 200, or 300, or 400 mesh/inch square grids), although the patterns of the mesh can vary [37-40]. More often the grids containing 400 squares per inch are used in SPA (Figure 3). Depending on the sample, a continuous thin layer of carbon film or perforated with irregular, termed Lacey grids, or regular holes (such as QUANTIFOIL) should be placed on the top of the copper grid (Figure 3) [37-40]. The type of grid selected in terms of the size/shape of the holes and distances between them is dependent on the sample. All these types can be used for automated and manual data collection.

The conventional procedure for freezing is the following [35,38,40]:

a. Drop of the sample (~3µl) is applied onto a grid, which was glow discharged to make its surface more hydrophilic, or hydrophobic, depending on the properties of the molecular complex under the study.
b. Sample is rested for a short time on the grid (0.5-2 min, depending on the sample).
c. Grid is maintained on the plunger.
d. Excess of the sample is blotted to make a thin layer of sample solution on the grid.
e. Grid is rapidly plunged into liquid ethane (or propane) that has temperature of -182 °C.

Ethane has to be cooled by liquid nitrogen in advance. Plunge-freezing in liquid ethane take place in ~10^{-5} seconds trapping the biological molecules in their native, hydrated state embedded in amorphous ice that has the same structure as a solid water. The amorphous ice does not have a crystalline structure. Cooling by plunging into liquid ethane is much faster than plunging directly into liquid nitrogen because liquid ethane is used close to its freezing point, so it does not evaporate and produces an insulating gas layer. This fast freezing prevents the formation of ice crystals and keeps samples at nearly native hydrated state and the process is known as vitrification of samples [33,35-38,41].

For the following cryo-EM procedures, the grids have to be kept at temperatures no greater than -170 °C, for transfer into the microscope using a cryo-transfer holder, and during the imaging, otherwise the amorphous ice will change it conformation and become crystalline, destroying the sample and contaminating the grid. Another important advantage of maintaining the sample at cryogenic temperatures is that the radiation damages induced by the electron beam will be significantly reduced when electrons pass through the sample [30]. More recently automated and controlled devices have been developed (Vitrobot (https://www.thermofisher.com/uk/en/) or Leica EM GP (https://www.leica-microsystems.com/products) [36], thus allowing higher reproducibility in grid preparation [38-42]. It is recommended that the first estimation of sample quality is made using the negative stain technique, which is fast, robust, and reliable [30]. It allows rapid assessment of sample quality, concentration, and suitability for the following cryo preparations.

3. Data acquisition

3.1 Direct Electron Detectors

During the last decade, digital detectors have enabled the direct detection of electrons without the intermediate step of transforming electrons into photons and then into an electrical signal

(Figure 4) replacing photographic films and CCD cameras. Direct detector devices (DDD) use an array of radiation hardened active pixel sensors (a pixel circuit) which are integrated into a silicon CMOS (complementary metal oxide semiconductor) chip [43-44]. In this case the electron energy is transferred directly into electrical signal. Another advance of this technology is that an amplifier is built into each pixel and allows fast signal readout from each single sensor (or pixel) nearly simultaneously (Figure 4) providing very high frame readout speeds [43-45]. This feature allows the possibility of recording an image during the overall exposure as a set of smaller sub-exposures. In cryo-EM it provides a valuable option for electron dose fractionation that is important in studies of radiation sensitive biological samples. Usage of the dose-fractionation is now provided by global direct detector technology. Depending on the detector type (Gatan, DE-Direct Electron, and Thermo Fisher Scientific) and available software, it is possible to record from just a few to hundreds of sub-frames per exposure [46].

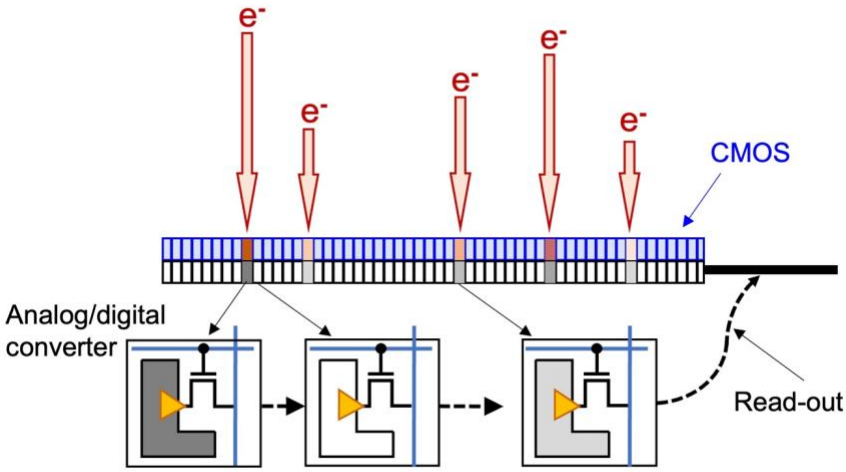

Figure 4. Digital cameras. In direct detectors active pixel sensor detectors, mostly based on CMOS technology, can capture the incident electrons [46].

The removal of the electron – photon transformation step and the fibre optics improves the Signal to Noise Ratio (SNR) on images registered by DDD. This can be best described in terms of the Detective Quantum Efficiency (DQE) [43-45]. The DQE is a measure of the efficiency of signal transfer by the camera and defined as a ratio of the SNR in the output image registered by the camera sensors to the SNR at the input image.

$$DQE = (SNR_{out})^2 / (SNR_{in})^2$$

The ratio depends on the spatial frequency (sizes of the details) of the image. A perfect detector would not distort the input signal and in an ideal system the output should be the same as the input. Therefore, the DQE of the ideal system would be equal to one for all

frequencies. However, cameras distort the fine details in images, and this is reflected by significant decline in the DQE at high frequencies [44-48].

Direct detectors allow registering electrons within high range of energies and are now used in 300 keV microscopes. The high sensitivity of these systems in sensing electrons has enabled scientists to create sensors of smaller size and coupled with improvements in software has offered a new mode in image recording which is known now as a counting mode. In this mode the system can record single electrons (this mode is implemented in K2, K3 (Gatan), Falcon 4 (Thermo Scientific™ Falcon™ 4), and DE cameras [46-50].

3.2 Micrograph sub-frame alignment.

Cryo-EM images recorded with DDD cameras (Falcon4 (Thermo Scientific™ Falcon™ 4), DE (Direct Electron) or K3 (Gatan)) represent sets of sub-frame images (movies) [51-55]. High rates of image recording can reveal the distortion of images induced by drift of the grid (sample) within the EM, which can be corrected by specifically designed procedures such as motion-correction [51-55].

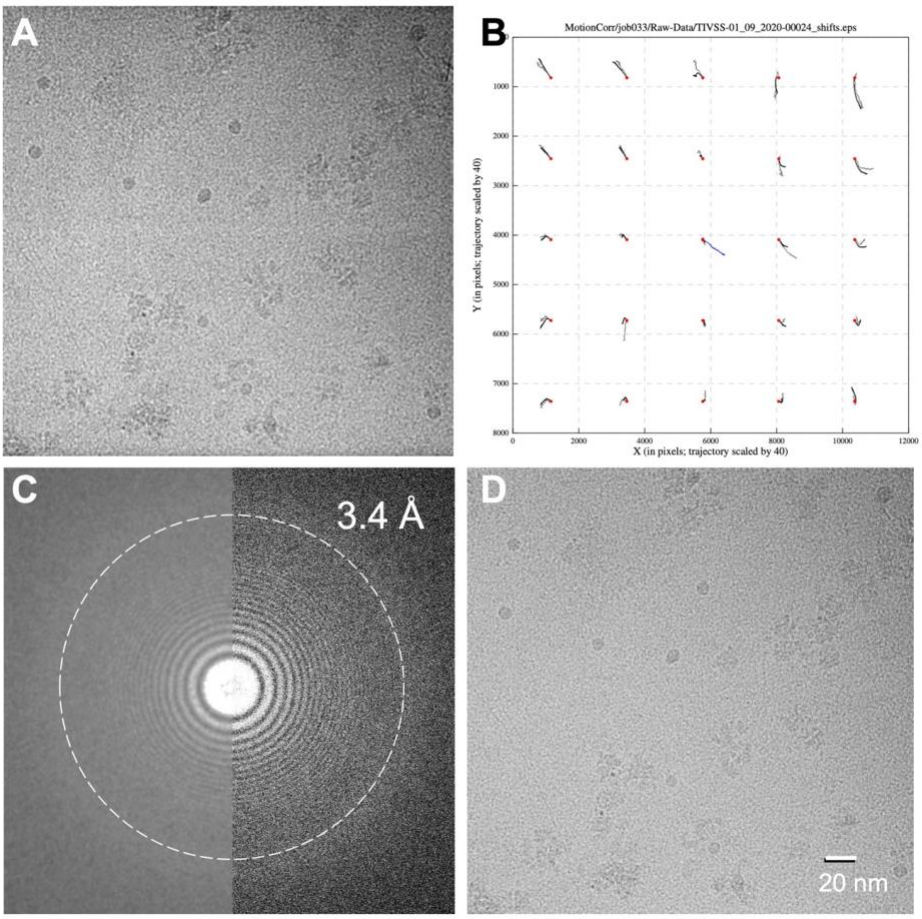

Figure 5. Cryo-EM images with motion correction. A. Representative cryo-EM image of vitrified T4SS particles (without motion correction). **B.** Motion of patches in X and Y directions in successive frames. **C.** Left: the power spectrum of movie frames summed without motion correction. Right: the spectrum after motion correction. **D.** Image after correcting the frame shifts. Protein is black in the cryo-EM images.

Typically, alignment of frames starts from frame N-1 that is aligned to the last frame. When these two images are aligned the corresponding pixels are summed, and frame N-2 will be aligned to this new sum. Then frames N-1 and N-2 will be summed and the frame N-3 is aligned to this new sum. The process is repeated in the same way towards the first frame. There are variations in algorithms when summation is done not for two frames for the following alignment, but for 4 or 5 frames or all frames. There are several algorithms for the motion correction of frame shifts that currently use alignments not of the entire image, but of regular lattice of smaller regions (for example 5x5 frame subareas). This approach helps to determine not only the translational shifts but also rotations of the frames under the beam [54,55]. Typically, the alignment is done starting from the last frames to the first ones since the characteristic features needed for the alignment are visible better on the last frames. Alignment is refined iteratively when on the next round of alignment, the total sum obtained during the previous round is used as a reference. The entire procedure improves firstly the signal-noise-ratio of the reference, and the iterative approach improves quality of the alignment. There are now a few software packages that can be used for the frame alignment. The image shown in Figure 5A represents the sum of the original frames without correction. The trajectory of the sub-area shifts during the successive exposures indicates that the movement of initial shifts of the sample is large at the beginning but then reduces, and different subareas move slightly differently (Figure 5B). A power spectrum from the sum of the frames without motion correction reveals that the Thon rings are fading rapidly due to the shifts in different direction indicated in Figure 5B. When the movie frames are aligned (after motion correction) the Thon rings became better defined and extend to nearly 3.5Å (Figure 5C, right panel). This signifies on the presence of high-resolution details in the images. Summation of the motion corrected sub-frames generates the final sharper image (Figure 5D).

3.3 Radiation damage

Images in EM are generated by the electron beam that illuminates the sample and then electromagnetic lenses form the image in the plane of the camera. While short wavelength electron beams significantly improve the image resolution of biological molecules it has been

demonstrated that bio-samples are very sensitive to high-energy electron irradiation that takes place during imaging [56-58]. Electrons are accelerated in the electron gun of the microscope and while the majority are only deflected by the electric field of the sample atoms (elastic scattering), some electrons collide and transfer their energy to the sample atoms (inelastic scattering). These atoms became ionized and therefore can cause X-ray emission, form radicals resulting in rearrangements of chemical bonds [56-63]. High energy electrons of the beam in EM may induce displacements, bond breakage and mass loss of low atomic number elements such as carbon, nitrogen, and oxygen [61,62]. These changes in biological complexes depend on the time of the overall exposure time to electron irradiation (cumulative dose) and were estimated using spot fading diffraction experiments on two-dimensional (2D) crystals and analysis of single particle images [59,61-63].

The resultant sub-frames of the image recorded with DDD cameras can then be used for specimen drift correction and usage of first part of the frame set to see the images of the object at the reduced electron dose. Typically, the images on the first two or three frames demonstrate large shifts of the sample, which reduces as movement slows. However, the last frames often indicate that the sample is damaged by the beam. A 3D structure derived from experiments where the sample has been overexposed can differ markedly from the structure of the native molecule. It has been shown using crystallography that exposure of crystals to X-ray induces decarboxylation of glutamate and aspartate residues, breakage of disulphide bonds and loss of hydroxyl-groups from tyrosine and methylthio group of methionine [61]. Bartesaghi and co-authors compared the density maps reconstructed from different fractions of the total exposure (10, 20, or 30 $e^{-}/Å^{2}$) [63]. Analysis of the high-resolution cryo-EM structures shows that densities for residues with positively charged and neutral sidechains are well resolved, while the residues with negatively charged sidechains were less resolved having weaker densities. Negatively charged glutamate and aspartate exhibit on average 30% less density than the similarly sized neutral glutamine and asparagine which is consistent with observations of X-ray analysis [59,61-63]. Therefore, the user can use all frames for the quality assessment of images and samples and only the first half or first two thirds of sub-frames (depending on the type of the DDD used in experiments) for the reconstruction of the native complex.

Cryo EM imaging has a major benefit in reducing radiation damages by keeping samples at cryo temperatures during imaging. Vitrified samples at liquid nitrogen temperatures preserve their native structure and should be imaged at these low temperatures, which increases

tolerance to ionizing radiation damage, since the free radicals generated from inelastic scattering events are unable to diffuse through the sample and cause secondary damage [57,58,61]. In addition, cryogenic temperatures (liquid nitrogen −195.8 °C) also restrict movements and the degrees of freedom of the molecular atoms after a bond is broken therefore limiting structural rearrangements induced by irradiation [60,61]. As a result, keeping and imaging samples at such low temperatures improves radiation tolerance from 2 to 6 times compared to room temperature imaging [60,62,63].

Other additional approaches that help to reduce the level of radiation damage include usage of low-dose mode during data collection [64]. Low-dose imaging is based on reducing the exposure time of the sample to electrons by focusing on an adjacent area that is sufficiently close to the area of interest but does not overlap it. "Search" mode requires a low-magnification overview image that is used to identify areas of interest while the "imaging" (or "photo") mode is used for actual data collection at high-magnification. The "focus" mode is set typically at the same magnification as imaging mode, but the beam is shifted to an adjacent area [65]. Such interchange between these modes is implemented in systems for the automated data collection and significantly allows reduction of radiation damages of the samples. Currently all electron microscopes used for biological studies come with pre-installed low-dose hard- and soft- ware allowing the efficient exchange between imaging modes.

4. Processing of 2D images

4.1 Contrast Transfer Function

The aim of single particle reconstruction is to provide an accurate representation of the three-dimensional structure of a molecule using a set of 2D image projection data. The frozen vitrified samples of macromolecular complexes are considered to be very thin objects so their images can be described as linear projections of the Coulomb potential of the molecular complex [30-32]. This approximation is used for the subsequent reconstruction procedure. However, images produced by the electron microscopes do not represent projections of the molecules under study. Deviations from the real densities of projections are induced by aberrations of the optical system of the EM microscope [65,66]. The effect of these aberrations on the registered image of the object is described by the function termed as the Contrast Transfer Function (CTF) of a microscope [30-32,65,66]. The CTF is defined by the type of electron source (beam coherence), the acceleration voltage that regulates the electron

wavelength, and aberrations of the objective lens (C_s, C_c, and astigmatism). The major factors affecting the CTF are the degree of spherical aberration (C_s) of the objective lens and a level of defocus (Δf). As a result, the CTF modulates the amplitudes and phases of the registered image. The effect of the microscope CTF can be clearly observed on a power spectrum (Fourier space) of the image registered by the camera, which demonstrates variations in the magnitude of the various frequency components of the image (Figure 6). The image contrast in EM micrographs depends on the operating conditions of the microscope such as the level of focus and aberrations. The overall effect of these factors on the image can be described in Fourier (diffraction) space (Figure 6 A and B) by the following equation:

$$F\{\psi_{obs}[\bar{r}]\} = F\{\psi_{sam}[\bar{r}]\} \cdot CTF(\bar{q}) \cdot E(\bar{q});$$

where $F\{\Psi_{obs}\}$ is the Fourier transform of the observed image; $\bar{r}$ are the distances in the images; $\bar{q}$ are spatial frequencies (Fourier space coordinate); $F\{\Psi_{sam}\}$ is the Fourier transform of the specimen; $CTF(\bar{q})$ is the contrast transfer function of the microscope; and $E(\bar{q})$ is an envelope function, which describes frequency-dependent attenuation of the contrast transfer function. $E(\bar{q})$ is related to the effects of various instabilities in the microscope, local spread in defocus, variation in the sample thickness, and specimen decay under the beam irradiation that lead to the loss of high frequency information (Figure 6C) [32,33,67].

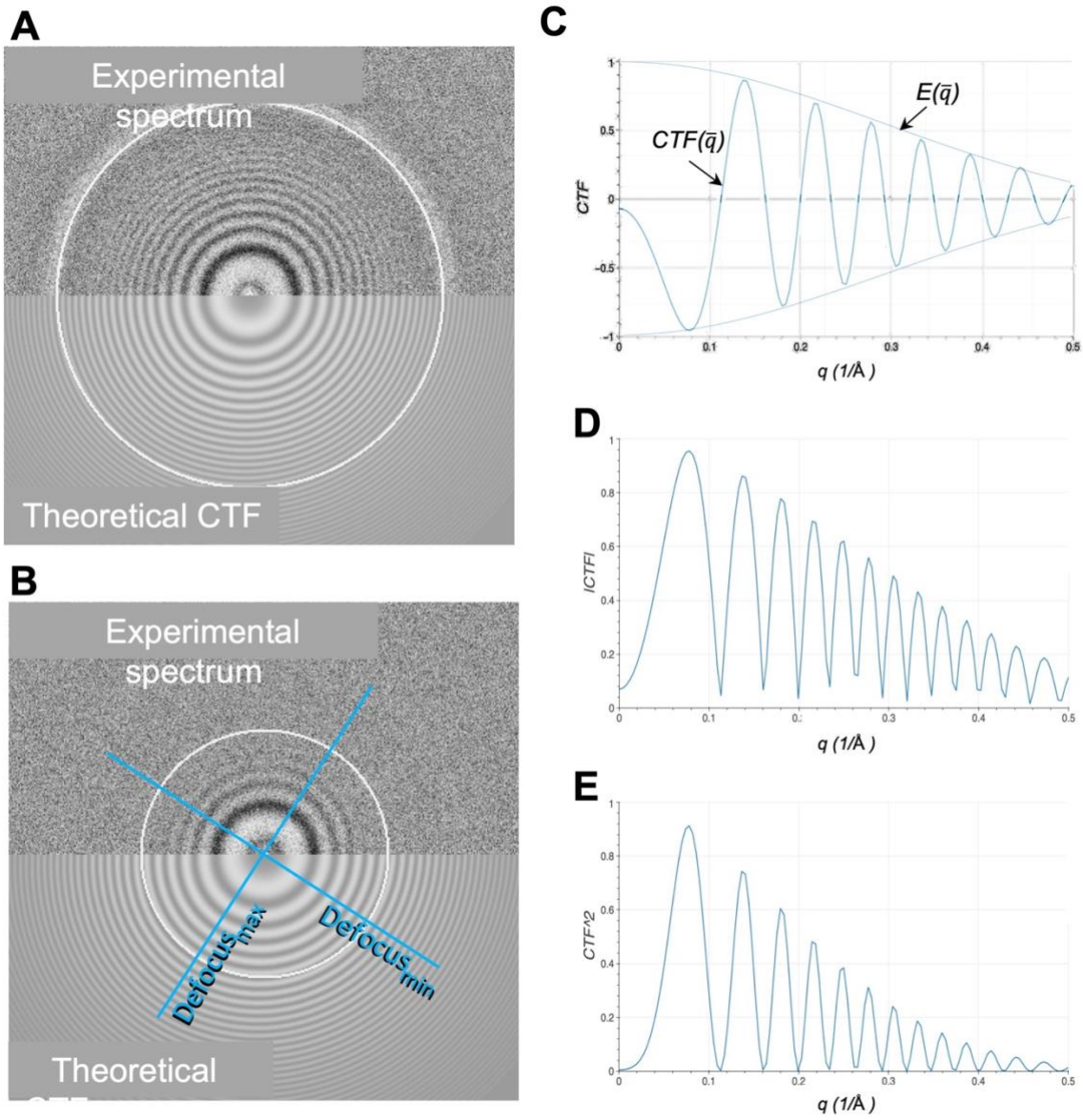

Figure 6. Contrast transfer function (CTF) and corrections. **A.** The CTF in an experimental spectrum (upper half of the panel). It is compared with a theoretically calculated CTF (bottom half of the panel). Image was taken relatively far from focus. For the accurate CTF determination the Thon rings from both parts of the images should match. **B**. Comparison of the theoretical and experimental spectra for the image taken closer to focus. Astigmatism assessment is done by measuring ellipticity of Thon rings ($Defocus_{max}$ and $Defocus_{min}$). **C.** The CTF oscillates changing the image contrast from negative to positive depending on frequency. Information is lost only where the CTF is zero. Dashed line shows effect of the envelope function on the signal transfer suppression at high spatial frequencies. **D.** CTF correction by phase flipping: negative lobes of the CTF are flipped over to positive. **E.** Noise suppression close to CTF zeroes by calculation of CTF^2

The major effects of spherical aberration of the objective lens on images of biological samples are phase changes and, therefore, alterations in the representation of densities. The CTF for the biological samples can be described by the formula.

Phase CTF = $-2 \sin [\pi (\Delta f \lambda q^2 - C_s \lambda^3 q^4/2)]$

where C_s is the spherical aberration constant; Δf the defocus; q the spatial frequency; λ the electron wavelength. The spherical aberration coefficient and the electron wavelength are the only constants and these values remain fixed for each electron microscope [30-32].

The effect of the CTF on the image appears as oscillations of the power spectrum that take the form of concentric bright and dark rings (named as Thon rings [65,66]). Dark regions show the positions of all zero crossings of the CTF, and bright regions correspond to areas where the CTF has large amplitudes that are either positive or negative (Figures 6C). The CTF limits the amount of information which can be obtained from electron images. At zero crossings of the CTF no information is transmitted, and specimen features corresponding to such spatial frequencies will not be visible in the final image.

Biological samples viewed in ice under close to focus conditions display very low amplitude contrast since the difference between their densities and that of water is very small [30,31]. Consequently, the images are typically taken far from focus (in underfocus mode) to increase the weight of low frequencies and thus improve the visibility of particles [30,31]. It is useful to remember that low frequencies are responsible for the overall shape and appearance of particles in images, while the high frequencies are related to the fine details. High defocusing (images taken far from focus) induces changes in the distribution of density information related to fine details which could be lost due to attenuation of amplitudes at high frequencies. The level of defocus used for imaging depends on the size of the bio complex. Images of small particles (~60-200 kDa) are often collected with a large defocus, sometimes up to 4-6 µm while viruses with diameters of 50nm and larger can be imaged at 0.5-1.0 µm.

4.2 Defocus Determination and Correction for the CTF effects

An EM projection image is only considered as a faithful representation of the registered projection of the object of study if it has been corrected for the CTF modulation effects of the microscope. To correct an image for the CTF effects and obtain the image that corresponds to the projection it is necessary to determine the defocus at which the image was taken and to assess it for astigmatism and drift. A nominal value of the defocus set on the microscope does not usually represent the actual defocus at which the image was recorded. Although the

acceleration voltage and the spherical aberration of the lens in the microscope are constant the typical deviations in sample thickness and variations in the hight of the supporting film in the holder will cause local deviations in defocus. As a result, the CTF that depends on the actual defocus should be determined for each image. Finding the exact defocus and level of astigmatism in cryo-EM images is of crucial importance when working towards producing a high-resolution structure.

The CTF determination is performed by calculation of power spectra (or amplitudes) of small patches (256 x 256 or bigger) from the average of all aligned sub-frames. The spectrum is then correlated with a set of theoretically calculated CTFs in a range of possible defocus values. The highest correlation between the observed and one of the theoretical CTFs indicates the actual defocus of the image and defines frequencies where the phases have to be flipped (Figure 6B, C). Different software packages for automated defocus determination are currently used which include: CTFIND4 (implemented in RELION and CryoSPARC), EMAN2, IMAGIC5, CrYOLO [20,22, 67-71]

Astigmatic images have power spectra that are not rotationally symmetric, and this can complicate and reduce the accuracy of the CTF determination. Generally, cryo-EM images which have greater than 5% astigmatism are not used for further processing. The level of astigmatism can be calculated as follows:

$$\text{Astigmatism} = (\text{Defocus}_{max} - \text{Defocus}_{min}) / \text{Defocus}_{avg}$$

Correction of the recorded images for the CTF modulation effects of the microscope are carried out in Fourier space after CTF determination of the image by multiplying the alternating bands of phases of the CTF (in a simplified option) by a square wave function which has the value of -1 at positions where the contrast transfer is negative and +1 where the contrast transfer is positive. This has the effect of reversing or 'flipping' the negative lobes of the CTF into positive contrast thus restoring the correct image phases (Figure 6D, E).

The missing information where the CTF crosses zeroes is restored by combining images at different defocuses so that where some images lack spatial information at a particular frequency others will provide the complementary missing information. High spatial frequencies are suppressed by the envelope decay, so amplitude correction is also important for maximising high-resolution details. This operation usually involves applying a Wiener filter to remove noise from the CTF [71-73].

4.3 Particle selection

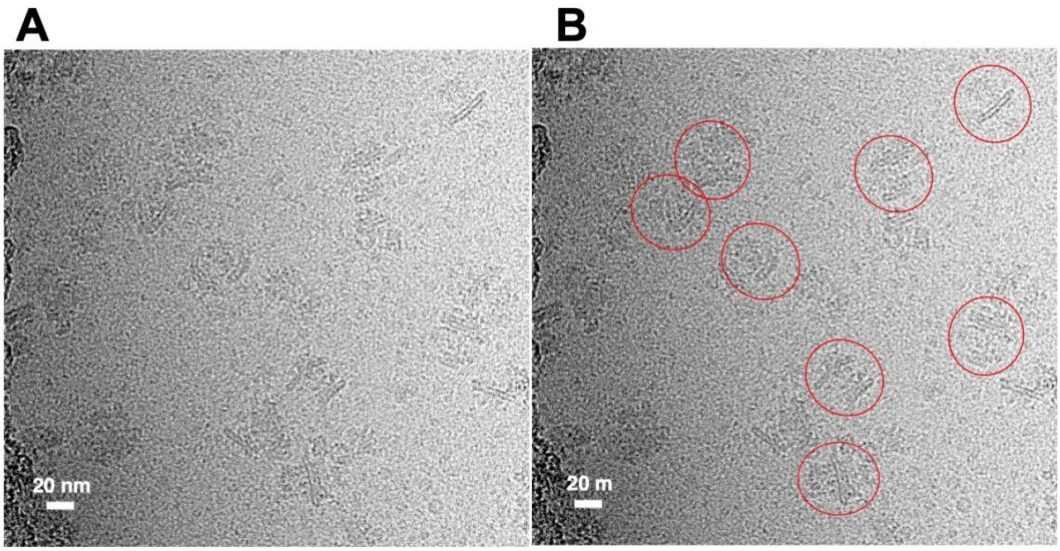

Figure 7. Particle picking. **A.** Cryo-EM micrograph of the R388 T4SS sample. **B.** Red circles designate examples of particles selected for the processing. The images were collected with a post-GIF K2 Summit direct electron detector (Gatan) operating in counting mode, at a magnification of 130,000 corresponding to a pixel size of 1.048 Å. The image has been taken far from defocus to increase the contrast and allowing visualisation of the lipidic bi-layer belt around T4SS transmembrane domains [Figure adapted from Ref. 28].

The structural analysis process in EM begins with selecting images of individual particles from micrographs. This involves defining their unique locations (x,y) within the image field and saving these coordinates in a data file that is used in the following steps of processing. This can be done using packages like RELION, CryoSPARC, EMAN2, Ximdisp, and some others [20-22, 69,74-80]. The initial approach often used is for the user to select single particle images by clicking on the image area that looks like a particle using a mouse. The coordinates of these points will be stored and then used to extract individual particles within a square box of designated dimension. The cut-out area must be large enough to retain some field around the object with some background. It is recommended that it should be twice the maximum size of the molecule under the study. Images of the selected particles must not be overlapping, squashed, distorted, fragmented or in direct contact with other particles. Particles can also be selected automatically with particle identification/picking programs such as Gautomatch, Autopicker, BShow, FindEM, blob picking [76-80]. These programs utilise the local correlation between a template (an initial reference) and a small image area (of the size corresponding to the size of the reference) to measure the degree of similarity between them. Areas which show maximum correlation with the references are boxed out. The poor contrast in ice images

and the presence of artefacts which could resemble target particles generally decrease the accuracy of automatic selection. New approaches for particel picking based on deep learning have been implemented in crYOLO, TOPAZ, and some other packages [71,81-83]. An example of a micrograph of vitrified sample of the T4SS core-outer membrane complex is shown in Figure 7

4.4 Normalization of data

Normalisation of all images is an essential pre-processing step. The contrast and intensity can vary from image to image during data acquisition even when all the EM settings are the same. This effect arises due to a few factors which include differences in the thickness of the carbon support film or ice, particle orientations, uneven staining, or merging images from different data collection sessions. Normalisation of particle images is done by setting the mean pixel grey value of each image to the same level, commonly zero and rescaling the standard deviation to an equal value for every particle image. Without normalisation the density variations such as very bright or very dark regions within an image can bias the cross-correlation procedures which are later used for alignment and calculation of particle classes. Typically, normalisation is based on the following formula:

$$\rho^{norm}_{i,j} = ((\rho_{i,j} - \rho_{avg})/ \sigma_{old})\, \sigma_{new}$$

σ_{old} and σ_{new} are the standard deviations of the original and target images respectively, $\rho_{i,j}$ is the density of a pixel in the image array coordinates .

4.5 Classification of particle images

To resolve problems related to radiation damages, signal/noise ratio, possible heterogeneity of the sample, presence of different conformation, and reveal structure/function relationship researchers a researcher needs to examine up to several millions of molecular particle images. The images extracted from micrographs should be examined for their quality, consistency of the molecular assemblies, and their structures represented in images. Manual inspection of this vast number of individual images is neither practical nor realistic since it is time consuming, and users are prone to errors and some subjectivity. Routinely, automated particle picking is followed by the 2D classification of selected particle data sets. The essence of this procedure is the comparison of particle images within a data set and cluster similar particle images into groups. Typically, 2D classification consists of several rounds. The initial step of classification aims to establish if images correspond to the object of interest or they represent fragments of micrographs mistakenly selected, disintegrated particles, unspecified blobs, bright spots, or edges of the carbon films. This step is often referred to as data cleaning. This

comparison is initially performed on a small subset of the data (just a few thousand images) and then gradually expanded to the entire data set eventually producing a few tens or two hundred classes. Visual inspection of classes is feasible and consequently allows the use images comprising selected classes in the next steps of processing. Images composing classes that are inconsistent in appearance (i.e., junk images not related to the sample) should be removed from subsequent steps of processing.

The next step is typically used to assess characteristic views of bio-complexes and initial distribution of their orientations. High percentage of classes having the similar appearance indicates strong preferences in the particle orientations. If the 2D classes do not demonstrate well-resolved features, it may indicate that a sample is unstable, or it overconcentrated and images contain adjacent particles that are overlapping with the central particle image, or the particles have strong specific interactions with the carbon support film, or with the water/air surface which produces a strong preference in the orientation of particles. Images comprising classes that have well-defined features and show different views have to be chosen for the 3D reconstruction analysis.

4.5.1 Principal component analysis

Principal component analysis (PCA) reduces the number of variables in order to find the most significant variations in the measurements [70,84]. The essence of the procedure is a transformation of a set of observations of possibly correlated variables (in our case images or reconstructed volumes) into a set of values of uncorrelated variables called principal components. In theory the number of the principal components should be equal to the number of original variables. However, since images contain a high level of noise the number of the meaningful components became much smaller. The principal components are described by the eigenvectors of the data matrix. PCA is the simplest of the true eigenvector-based multivariate analyses [70,84]. It is now used in the 3D classification (24).

4.5.2 Maximum likelihood estimation

Maximum likelihood estimation (MLH) is a method that assesses parameters that would correspond to a statistical model [85]. When applied to a data set (such as the image data set) and given a statistical model (the initial 3D model), MLH provides estimates of how another new reconstruction would correspond to the suggested model and what sort of deviations could be observed. This concept can be rephrased: once a model is specified in relation to a certain set of parameters (e.q. such as orientations, positions of the mass centre, distribution

of domains, and overall sizes the MLH evaluate how well the suggested model fits to the data collected (EM images). The quality of this correlation is assessed by finding parameter values of a model that best fits the data - a procedure called parameter estimation. In the EM case that would be a 3D model that maximally corresponds to the data set otherwise the model has to be modified. If there are several models, then the data set will be divided during processing into groups corresponding to the models. MLH has many properties that should be taken in account during estimation, these include sufficiency (complete information about the parameter reflecting features of interests); consistency (numbers of images relating to this or other 3D models), efficiency (the lowest-possible variance of parameter estimates), and could be other practical parameters [85-88]. This MLH method is used in the analysis of 3D reconstructions and implemented in RELION [20].

4.5.3 K-means

Cluster (or classification) analysis is a tool to identify groups of similar objects. This type of analysis is used for grouping similar images (particles in the same orientations). The aim of the K-means approach is to create groups (classes) of data subsets that are as similar as possible while also keeping the classes as far (different) as possible [89,90]. It ascribes data objects to a class in such way that the sum of the squared distances between the objects and the centroid of the class (arithmetic mean of all the sub data in this group) are at the minimum, and the distances between members of the class are minimal. The lower variations within the classes, the more similar are members of this group of the data set. The starting points are selected at random and named as the seeds. The seeds should be placed as far from each other as possible. The next step is to take each point belonging to a given data set and associate it with the nearest centroid. Averages are calculated for each class (initially using a subset of the data) and the distance between each image and the obtained averages are calculated. A new class will be formed by the images that were the closest to one of the averages. Then the class averages are recalculated again. This process is done iteratively with increasing numbers of images used for calculations of averages until the images cease to move between classes [89-91]. In this method (used in RELION, XMIPP, EMAN [20,21,23,69]) the user defines a number of classes as K, it is often not bigger than ten, but with improved algorithms and GPU usage, up to 200 classes can be defined (see the last versions of RELION). Here the algorithm randomly assigns at the beginning a few images as initial classes [20], the next step increases the number of images, compares them with the initially selected images and calculates the averages. The iterations include gradually

increasing the number of images and reassessments of distances between images comprising the averages and distances between the averages. The K-means method is reasonably fast, and it works better in low dimensional space since dimensionality increases the time and a local minima problem may occur. If we are using several millions of images the last iterations may take significant time. However, the multi-processor computers can help to make this task sufficiently rapid.

4.5.4. Modification and new developments in classification.

Processing cryo-EM image data to reveal heterogeneity in the protein structure and to refine 3D maps to high resolution requires analysis of large data sets. The stochastic gradient descent (SGD) and branch-and-bound maximum likelihood optimization algorithms permit the major steps in cryo-EM structure determination to be performed in significantly shorter time. Furthermore, SGD with Bayesian marginalization allows ab initio 3D classification, enabling fast automated analysis and identification different conformations of protein complexes without bias from a reference map. These algorithms are implemented in CryoSPARC [91,22].

Recently new approaches have been suggested for the fast classification of images that are based on usage of denoised images. The essence of these methods is based mainly on three techniques: spatial filtering, temporal accumulation, and deep learning. Deep learning uses a neural network to reconstruct the signal. The neural network is trained using various noisy and reference signals such as data from known test objects that can be applied to the new data [22, 91-95].

4.6 Determination of particle orientation

In order to obtain the 3D structure of a biocomplex from EM images, the orientation of each of the individual particle image must be determined. The location of an individual molecule can be identified by X,Y,Z coordinates and the shifts of different particles with respect to each other can be described in the same way as shifts in X,Y, and Z. The particles can also be rotated by α, β, γ angles that are defined as Euler angles. This means that a molecule has six degrees of freedom in space. In the microscope projection images are taken along the Z-axis of the translational system of coordinates, therefore the shift in Z direction is not significant (we assume that the electron beam is parallel) but the shifts in the X and Y directions need to be determined. During translational alignment, the centre of the molecule is set to X=0 and Y=0. In order to calculate the 3D map from individual images or class-

sums, it is necessary to determine the orientations of the characteristic views (classes) relative to each other.

The angular distribution of different images should evenly cover the Euler sphere or the asymmetric triangle (the independent asymmetrical part of Euler sphere for particles with symmetry). This is essential to achieve an even representation of all details in the structure, or at least a set of images chosen for the reconstruction should have such a distribution of angles that cover a big circle of the Euler sphere [96]. If the distribution of angles is patchy this leads to the appearance of stripes in the 3D electron density map. The size of the trustworthy details that might be resolved can be assessed using a formula derived by A. Crowther [97] assuming that projections are evenly distributed:

$R = D/N$

N - number of views, D - diameter of particle, R - target resolution. The N number can be significantly decreased for the same resolution if the complex has high order of the point group symmetry.

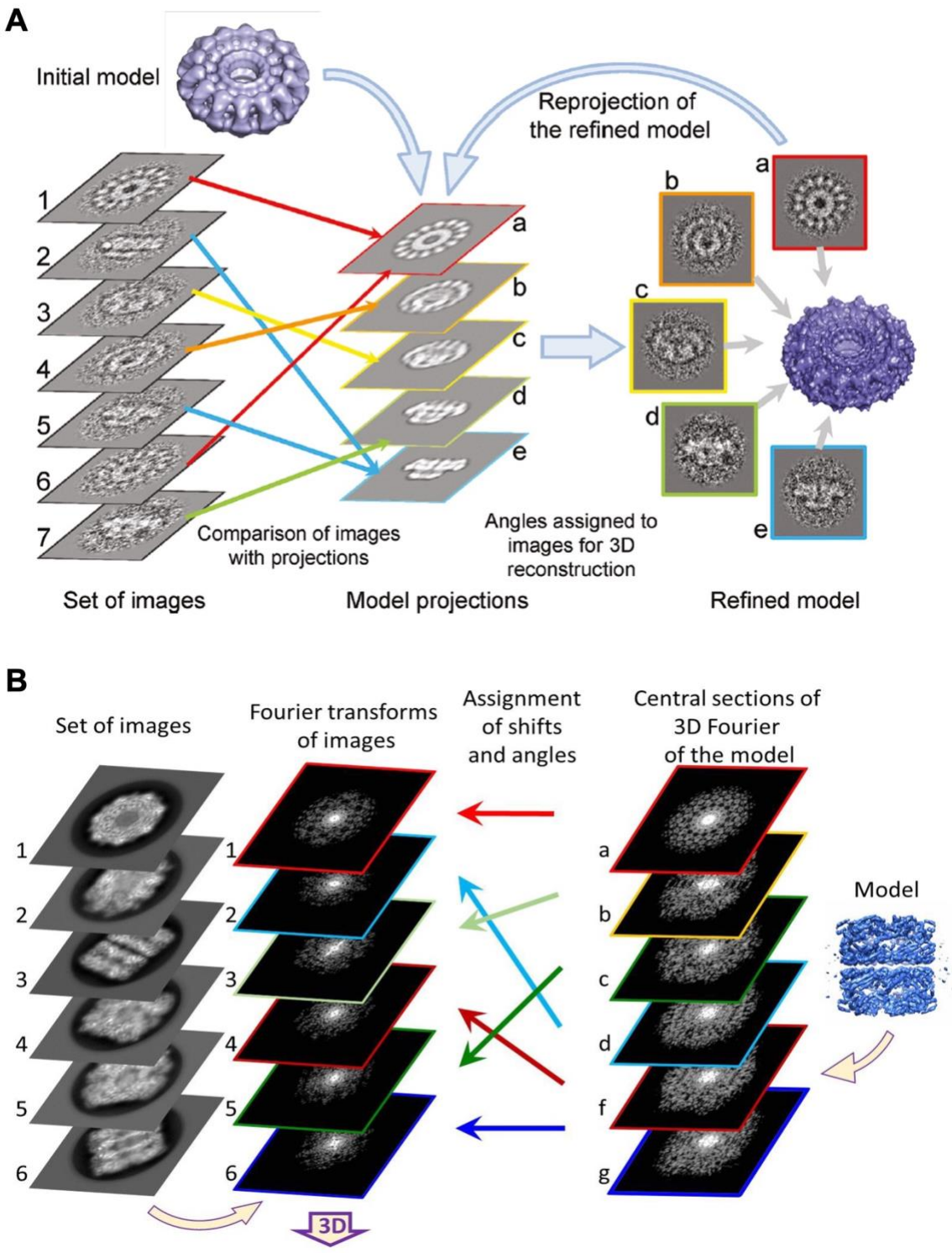

Figure 8. Projection matching procedure. A. Projection matching in real space. A set of images is compared to a set of references calculated from an initial model (low resolution). Once the best match is found between the image and one of the model projections, based on the height of the correlation peak, the shift relative to the matching reference and angles of that reference are assigned to the image. Images 1 and 6 have the best correlation with model projection a (red arrows), while images 2 and 5 match image e (blue arrows). Image 3 corresponds to the tilted view c (yellow arrow). A new 3D map is calculated using images with the assigned angles. The refined 3D

reconstruction is then reprojected with a smaller angular increment to generate new references for the next iteration of refinement. **B**. Projection matching in Fourier space. Fourier transforms are calculated from a set of images and compared successively to a set of central sections of a 3D Fourier transform from an initial model. Once the best match is found between the FT of the image and one of the references, based on the height of the correlation peak, the shift relative to the matching reference and angles of that reference are assigned to the image. A new 3D map is calculated using the FT of images with the assigned angles. The 3D FT is calculated from the refined 3D reconstruction and the new central sections are used as references for the next iteration of refinement [12].

4.6.1 Projection matching

Projection matching requires an initial model and it is based on a simple principle of comparison of the images with projections of the model (Figure 8) [30]. As a 3D template (an initial map), one can use the low-resolution negative-stain EM 3D reconstruction, the low-pass filtered X-ray model, or the EM map of a homolog. This template is projected in all possible directions covering the entire Euler sphere with a certain angular increment. Then the images or class averages of the data set are compared with these references, and the angles corresponding to the reference with the best cross-correlation will be assigned to the image [12]. Projection matching helps to determine the out of plane rotations of the object. During the angular refinement, the angular increment between projections of the model is reduced, or more projections with a small increment can be calculated around the initial angle, so the orientation angle will be more accurately defined. This method is easy to use, however, it is extremely time-consuming due to the long computation during which it is necessary to try all possible in-plane alignments and to compare each image to a set of references. Nonetheless the usage of multi-processor computers helps to speed up the process. Once the Euler angles are assigned to all images or class averages, a new 3D reconstruction will be calculated, and a new set of refined higher resolution model projections will be computed for the next round of projection matching.

Projection matching can be done both in real space (space of projection images) and in Fourier space (Figure 8) [30, 97,98]. Software packages currently favour Fourier space due to the advent of fast algorithms to calculate correlations between images and model projections. Most current programs such as RELION, CryoSPARC, EMAN2 are based on projection matching procedures which are performed in Fourier space [20,21,22,69].

4.6.2 Angular reconstitution

The EM images represent projections of embedded molecules in random orientations. If there is no initial model, the angular reconstitution technique is the method of choice to determine

the relative orientation of images. The common line projection theorem postulates that every pair of 2D projections of the same 3D object has, at least, one mutual 1D line projection that is called a common line projection [70,99,]. Thus, matching of 1D line projections for different images allows to establish the relationship between the 2D projections and determine angles between the common lines and, therefore the relative Euler angles of the images.

It is also possible to determine orientations using common lines in Fourier space [97,98,100]. The theorem of the central section states that the 2D Fourier transform of a 2D projection represents a 2D central section through the 3D Fourier transform of the 3D density. In Fourier space, a common line corresponds to the cross-section of Fourier transforms of images. It means that two Fourier transforms from two different 2D projections of the same 3D object have at least one common central line [97,98,100]. Here a comparison of the radial lines of the Fourier transforms of one image with all possible radial lines of the Fourier transform of the other image is performed. Again, similar to the real space, the angle between common lines of the two images with respect to the third one gives the angle between these two views.

5. 3D analysis of EM structures

EM images are considered as 2D projections of the 3D object [30,101-104]. This is due to the large depth of focus in TEMs. The depth of defocus is related to the acceleration voltage: the higher voltage the greater the depth of focus which can be up to 200 nm. Therefore, the image should represent a projection (the total sum of electron densities along the beam rays) in the image plane produced. However, for the images to be considered as projections, they have to be corrected for the CTF effects (see above). Once the CTF correction is done, and the Euler angles have been assigned to each projection image, then the 3D electron density for the particle can be determined.

Several approaches are used to calculate 3D densities of the molecules from their projections. Since the current trend is towards complete automation of the image processing, two approaches are now commonly used in EM due to the efficiency of their implementations. One is where the reconstruction is calculated in Fourier space; the other performs reconstructions in real space and based on the filtered back-projection algorithms [12, 30,101-104].

5.1 3D reconstruction in Fourier space.

This approach is based on the theorem which states that the Fourier transform of a 2D projection of a 3D object constitutes a central section of the 3D Fourier transform of the object [97,98]. This means that the Fourier transform of projections from different angular views can be merged to fill up the Fourier space with different 2D sections that are calculated from the images. Recovery of the 3D structure of the object in real space is done by reverse transformation of its 3D Fourier transform (Figure 9) [100,101,104,105].

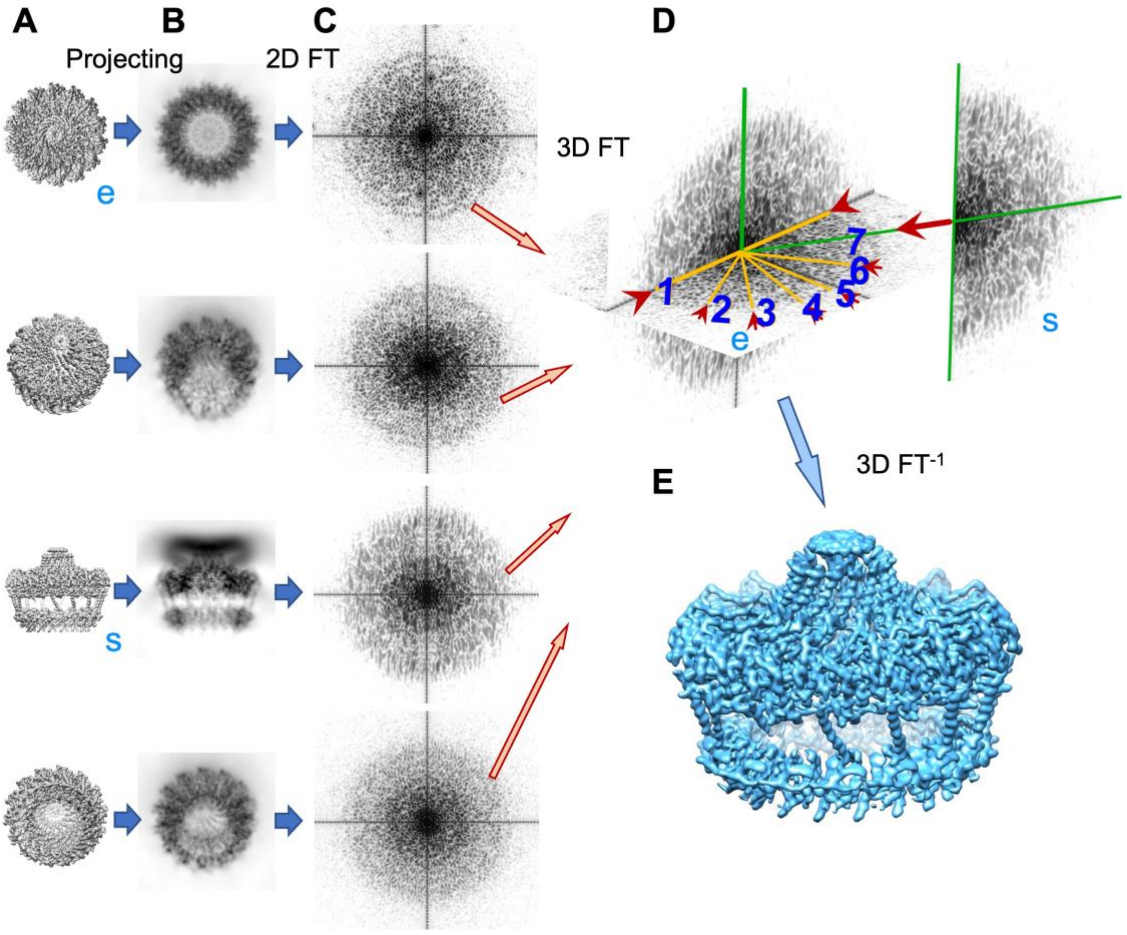

Figure 9. **Reconstruction using Fourier transform of images.** **A.** T4SS outer-membrane core complex (14-fold symmetry) is observed in different orientations on the supporting film. **B.** Projections of these particles that are equivalent to EM images in the direction of the electron beam. **C.** Fourier transforms (2D FT) of the projections shown in **B**. **s** – is the FT of the side view and **e** - the FT of the end view. The corresponding Fourier transforms of are shown in the panel **C**. **D.** 2D transforms that share at least one common line in reciprocal space. Common lines between the side view projection(**s**) and the end view projection (**e**) are shown in green lines. Orange lines indicate common lines between symmetry related side projections. The angles between pairs of common lines determine the relative Euler angle orientations. **E.** An inverse Fourier transformation of the combined 2D transforms generates an improved real space structure seen as electron density.

In Fourier space the large number of central sections used causes them to overlap at and close to the point of the origin. This leads to overweighting of the low frequency components in the Fourier transform and to the effect of blurring similar to the simple back projection in real space. So currently used algorithms based on Fourier methods employ down weighting of low or high frequencies by applying a weighting filter to the resultant map.

5.2 3D reconstruction in real space.

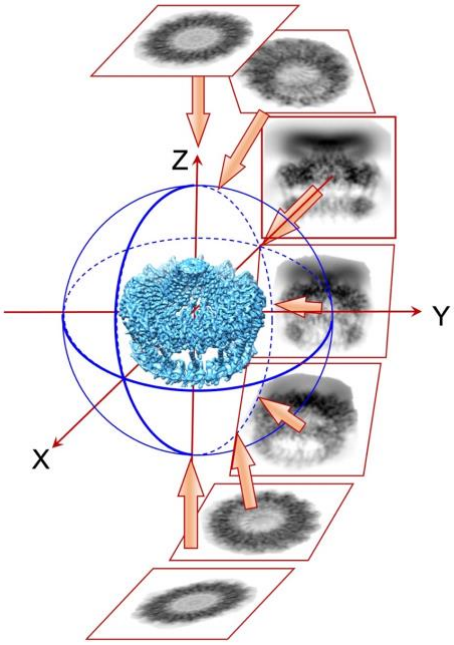

Figure 10. **3D reconstruction in real space**. Different images of the core OMC are shown and situated around the Euler sphere. Each particle image is back projected along its assigned Euler angle in real space. As the back projected density from each class average intersects the 3D electron density of the entire object, it is captured as a 3D map.

These methods calculate the 3D distribution of densities in the space of the object (Figure 10). The exact filtered back projection algorithm is implemented in many software packages related to EM tomography [102,103]. In this method each image of the data set (or classes) is stretched along a direction defined by the determined orientations of images. Electron densities in 3D are obtained by summation of rays from stretched projections. The electron density generated by these summations produces densities for each voxel. As more projections are included in the 3D reconstruction the voxels become better defined (Figure 10F). To avoid additional low frequency background induced by the procedure of projection stretching, images are filtered in advance (although in some packages the filter is applied to the resulting 3D reconstruction). A high pass filtering of the input 2D projections corrects the overweighting of the low frequency components thus restoring amplitude balance and so blurring is minimised.

5.3 Structure Refinement

All single-particle EM packages use nearly the same procedure for the refinement of structures after the first 3D model has been obtained (Figure 1). It is done by realignment of single-particle images with new references obtained from the new model. It is often

combined with determination of angles: projection matching using a smaller angular increment and/or a local refinement of the angles [12,98,99]. The new 3D model is used to calculate a fresh set of re-projections the number of which is increased according to the reduced angular increment. This enlarged set is used in projection matching to refine the orientation of the particle images. As soon as new angles are determined they are assigned to the images that have the best correlation with the model projections. While all implementations share the same principles of refinement, the details of the algorithms and the degree to which the user can control the process vary significantly .

5.4 3D classification for analysis of heterogeneity molecular complexes

The dynamics of structural changes can be assessed quantitatively using an iterative 3D classification procedure, which is based on one or a combination of 3D PCA, SDG, K-mean, MLH approaches [22, 23,24,70, 85-88,91,106,107] (Figure 1). The structures obtained can be ordered according to the degree of their conformational changes according to the values of the principal components or extent of displacements between corresponding domains. This aids the visualisation of motions involving flexible domains enabling determination of their phases and links to other domains within the complex. Evaluation of the particle numbers that correspond to each conformation allow quantitative assessment of the probability of the intermediate states. The best-resolved regions of the structures typically correspond to more stable elements where more flexible or peripheral components have significantly lower resolution.

There are several new packages such as cryoDRGN (Deep Reconstructing Generative Networks), which uses a method for heterogeneous cryo-EM reconstruction based on deep neural networks. The neural networks, which are known for their ability to model complex, can learn to identify heterogeneous ensembles within cryo-EM maps. It has been shown that a representation of structure by this approach can model density maps at high resolution as precursors, before revealing the full cryoDRGN framework usage for unsupervised heterogeneous reconstruction analysis [18,19,22,88,94].

6. Evaluation of the structure quality

When the map of a new structure is obtained, the molecular mass and its oligomeric state should be estimated. The map needs to be inspected at a 1σ threshold of density level (that may vary depending on the software used) that corresponds typically to the molecular weight

of the complex in the study. If the complex consists of several interacting proteins the map should not have disconnected fragments of densities, they should be continuous as well as above the background noise. The concept of resolution is based on assessment of the minimal distance between two points in the image at which they can still be distinguished from one another. That criterion was formulated as the Rayleigh criterion: when the centre of a peak of a one-point image falls exactly on the first zero of the second point [108]. In electron crystallography, the signal-related Fourier components of the image are linked to the reflections on a regular lattice, the reciprocal lattice, and a resolution is defined by the frequencies of the reflections that are above background noise and therefore available for the Fourier synthesis [108]. This crystallographic resolution R_c and Raleigh's point-to-point resolution distance d are related by $d = 0.61/R_c$. How can this be done in an objective manner in single particle analysis? For several decades we have used the concept of Fourier shell correlation (see below). However, during the last few years due to the tremendous achievements of single particle cryo-EM several modified approaches have been suggested, and these methods of the resolution assessment became closer to the criteria used in X-ray crystallography.

6.1 Fourier shell correlation and the Gold Standard approach

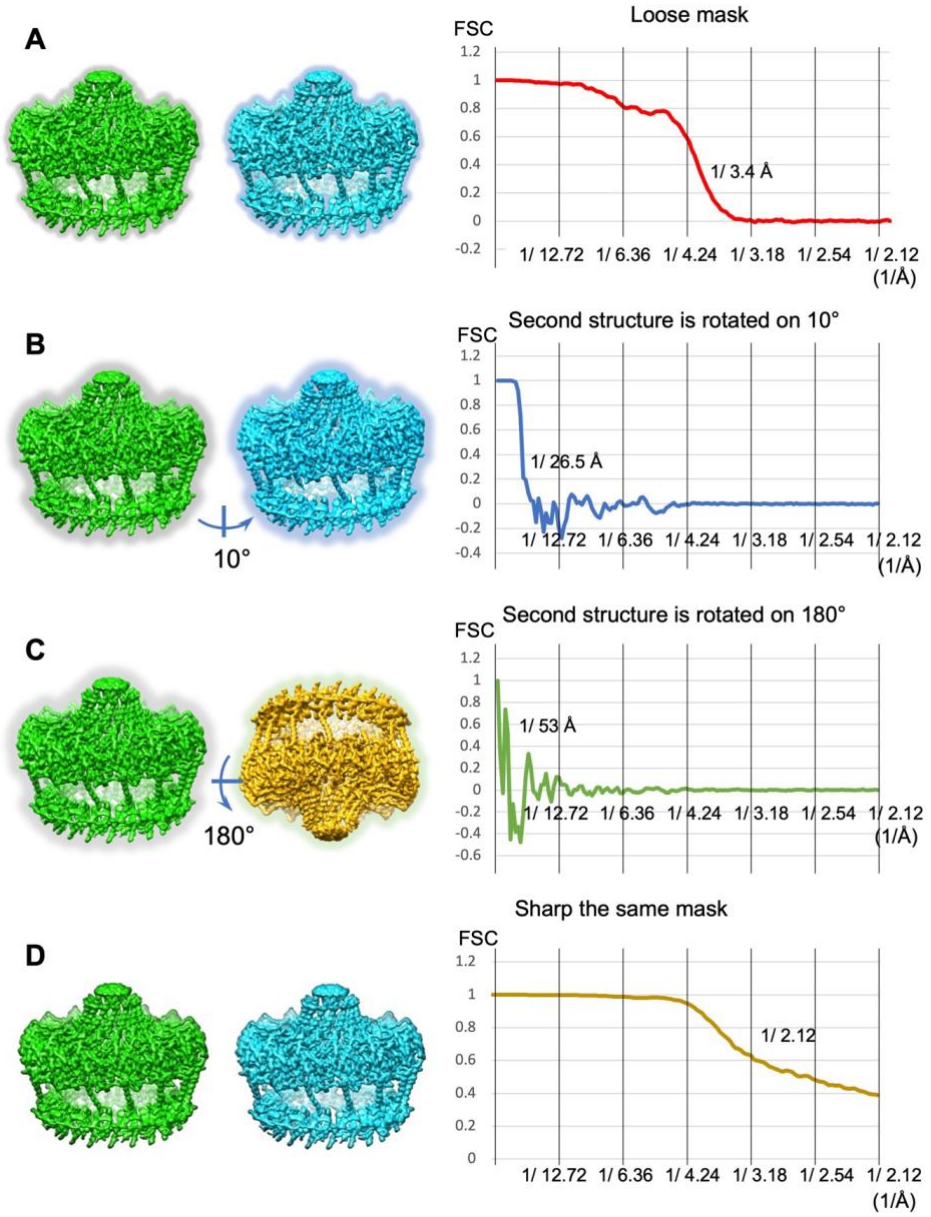

Figure 11. Examples of Fourier shell correlation (FSC) and resolution assessments. A. FSC curves for two independent 3D structures that have been aligned and masked with a loose soft mask shown as a halo around the particle images. A resolution assessed at the 0.143 level is 3.4 Å. **B.** The second structure is rotated by 10° around the rotational axis. While the overall shape still coincides well small details are no longer in the register. This is reflected in the FSC curve which falls rapidly, and the resolution is only 26.5 Å. This corresponds to the size of major domains within the structure. **C.** The structures are not aligned. FSC falls even more rapidly and indicates only the consistency in the overall sizes ~ 53 Å. **D.** FSC between two aligned 3D structures with the same tight mask. Good correlation at high frequencies indicates on the correspondence between masks imposed on the structures and therefore, a resolution is overestimated.

In single-particle analysis there is no well-defined periodical pattern in the Fourier spectra. Common practice is to look for data consistency by splitting the data set randomly in half and comparing the two resulting averages (3D reconstructions). The resolution of a 3D map (a

size of the reliable details) can be assessed by Fourier shell correlation (FSC). Two Fourier transforms are calculated, and the corresponding spherical shells are compared using normalised cross-correlation as a function of spatial frequency (R) (radius in the Fourier space). The value of the cross-correlation is used to assess at which frequencies (or level of detail size) these two maps begin to differ. It important to note that the resolution implied by Fourier shell correlation (FSC) resolution depends on how the data were divided and which threshold of FSC has been used for the assessment. Previously it was considered if the correlation falls below the 0.5 threshold, then the details are different [109]. Currently, there are several criteria to determine the threshold used in FSC and nowadays the threshold of 0.1432 has become increasingly popular, since it is closer to the measurements used in X-ray crystallography [110-111]. Scheres and Chen proposed a "gold standard" method for evaluation of structure quality [111]. According to this approach, the initial dataset is divided into two halves from the very beginning, and two models are refined independently. This approach helps in the refinement of structures to avoid biasness towards the same model used for the alignment and determination of angles. Once the structures have been obtained, the FSC curves can be determined as usual. If one would like to compare the structure obtained with some other known structure it is critical that both structures should be aligned for a correct FSC estimation (Figure 11).

The main disadvantage of FSC is that for the resolution assessment it is required to divide data into two halves and that significantly reduces the data set used for the final 3D reconstruction. An alternative approach for the evaluation of the reliability of details in 3D reconstructions (using the complete data set) is the randomisation of phases (or the randomisation of both randomisation of phases and amplitudes) above the frequencies critical for the assessment of details. The main concept of the approach is to modify an original data set of particle images in such a way that the amplitudes and phases beyond a certain chosen frequency are substituted by random values. This randomisation of phases (and sometimes amplitudes) at high frequencies is equivalent to the replacement of high frequency structural details by noise. The modified data set is subsequently subjected to the same image processing procedure used for the original experimental data. The FSC between these two structures usually demonstrates a sharp drop at the same frequency where the substitution of phases and amplitudes has occurred [112]. Any non-zero FSC values beyond the resolution where the noise was introduced reflects a level of bias during image processing. It is important to note that data sets with high frequency noise contains little information about the

real structure compared to the original data set. This may mean that particle orientations will be less accurately defined and may affect the value of FSC at the frequencies close to the selected threshold chosen for the phase substitution. 3D masking may also affect the behaviour of the FSC curves at high frequencies. The FSC can be improved if the featureless regions are masked out. A tight mask with a very sharp boundary can produce strange artefacts in FSC such as increasing up to the highest frequency defined by the sampling of images (Nyquist frequency, https://www.gatan.com/nyquist-frequency) indicating that details in the structure are related to the mask but not to the sample structure. (Figure 11).

6.2 Local estimation of resolution

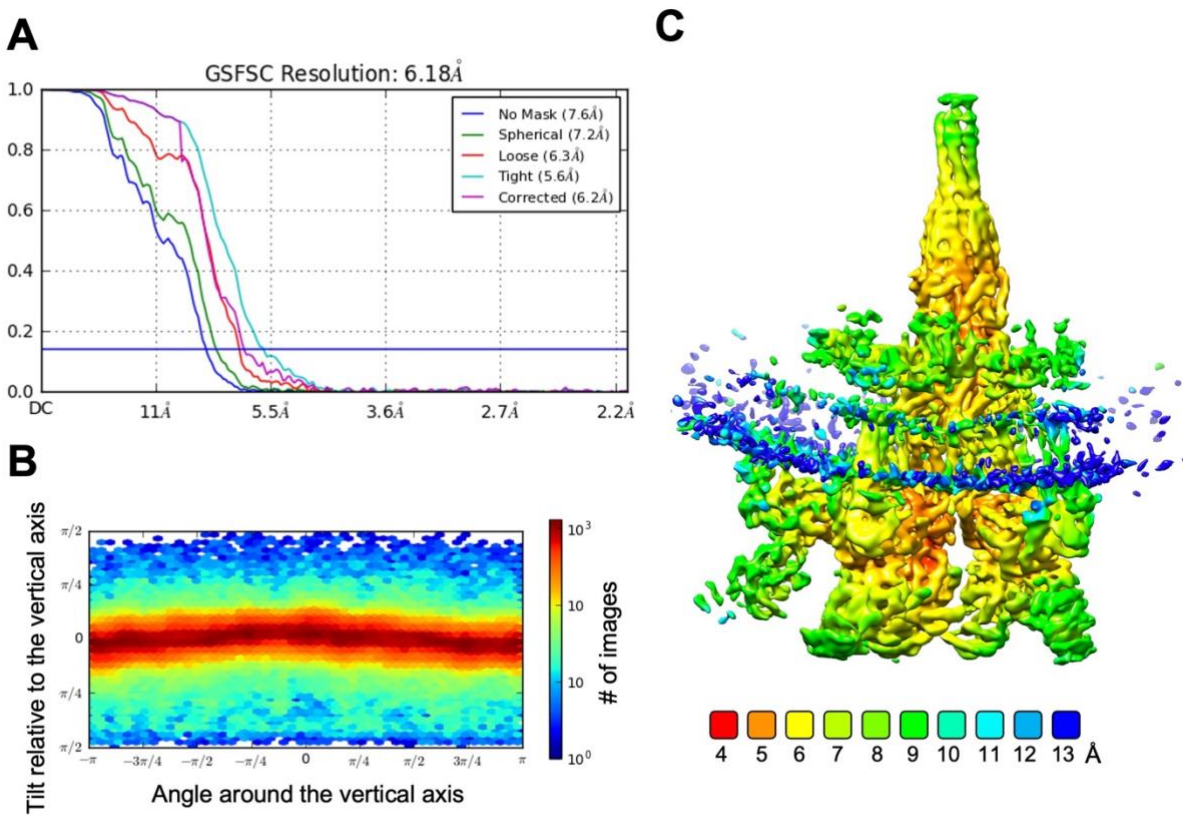

Figure 12. Local resolution of IMC-Arches-Stalk domain of T4SS [EMD-13767, 28]. **A.** The overall resolution derived from Fourier Shell Correlation (FSC). FSC curves show the correlation between two independently refined half-maps as a function of frequency; the various curves are colour coded as follows: without masking (blue), spherical mask (green), loose mask (red), tight mask (cyan) and corrected (purple). A cut-off 0.143 (blue line) was used for resolution estimation. **B.** The angular distribution of images used during refinement of the IMC-Arches-Stalk structure. **C.** The density map is coloured by local resolution (σ = 0.06). Local resolution was calculated using CryoSPARC and coloured as indicated in the table below the map. The values indicated are in Angstroms. [Figure adapted from Ref. 28]

Another approach that has become popular during the last years is resolution analysis of the 3D density maps obtained from the whole data sets through computing the cross-correlation between neighbouring voxels in the Fourier domain. The ResMap algorithm [113] is based on assessing a local-sinusoidal model at $r = 2d$ (where d is the voxel spacing in Å) that has the best fit within a small window of the image. As the small window moves through the map the Fourier neighbour correlation computes the correlation between neighbouring voxels in the Fourier domain and the sinusoidal model [113]. The likelihood ratio tests are conducted for all voxels in the volume. At a fixed wavelength equal to d, the standard likelihood-ratio test can detect whether a local-sinusoid is a meaningful part of the model approximation. The test requires an estimate of the noise variance, which can be evaluated from the region surrounding the structure. The smallest r at which the likelihood-ratio test passes at a given p-value (probability) defines the resolution. The p-value is the measure of whether the outcome of the test is due to an actual effect or mere a random chance. Voxels that satisfy the test are assigned a resolution r, while those that fail will be examined at a larger r (bigger wavelength of the sinusoidal model). The algorithm produces a local resolution map with a resolution assigned to every voxel in the density map (Figure 12).

7. Interpretation and fitting of atomic models

Final verification of the quality of the obtained EM map, is done by analysis of the quality of fitting of known atomic structures, homologous atomic models, or results obtained by *de novo* tracing of the polypeptide chain into subunits or protein component domains. Previously, the resolution of most density maps produced by SPA was between 20 Å to 30 Å. At such a low resolution, large domains can be recognised according to their overall shape. This level of detail does not provide sufficient information relating to the interaction between proteins and possible active sites for example or the locations of specific domains in multi-domain assemblies. The usage of antibodies and different methods of labelling specific domains, or construction from reasonable pseudo atomic models based on the EM maps themselves, however, have allowed their identification and positioning. Nonetheless, additional (often substantial) biochemical research is required to verify interpretations. In sub-nanometre resolution maps (6 Å to 9 Å range) densities corresponding to α-helices are characteristically cylindrical with an obvious "twist" that aids accurate fitting and the determination of overall structural handedness. At 4.5 Å, β-strands in β sheets begin to

resolve while at 4 Å, densities corresponding to large amino acid side chains become visible. At resolutions of ~ 3.7 Å or higher, the *de novo* tracing of polypeptide chains can be performed using methods developed in X-ray crystallography [114-116]. The highest resolution achieved using cryo-EM has currently been reported as approaching 1.5Å where the atoms of individual amino-acid are visible [1-7].

An efficient approach is when pseudo atomic models obtained by homology modelling are fitted into cryo-EM density maps to build atomic models of the individual proteins. The basic principle of the fitting procedure is assessment of the correlation between a density map and the model. The optimal cross correlation between the EM map and modelled densities of the atomic structure localises the best fit of the model. Such fitting is performed using the maps at a resolution greater than 3.7 Å. Depending on the software used the search can be accomplished in reciprocal or real space. The initial stage of the fitting procedure is carried out manually or automatically as a 'rigid-fit' if a homologous model exists. These can be constructed using the programs Phyre, I-Tasser, RoseTTAfold and AlphaFOLD2 [117-120]. Regions of the protein that are naturally flexible and do not immediately fit into the electron density can be adjusted manually in Chimera [121] or Coot [122] or in a more automated manner using FlexEM [115], IMODFIT [123] or other available packages. The flexibly fitted structure can be optimised and checked for clashes using Phenix [124]. This last step allows fixing the positions of secondary elements while simultaneously applying geometrical restraints.

There are specific strategies that directly relate to the fitting of homology models [125] into EM density. EM-IMO (electron microscopy – iterative modular optimization) methods allow the refinement of protein models based on homology modelling [126]. These methods endeavours to build, modify and refine the local structures of protein models using cryo-EM maps as constraints. A multi-parameter refinement strategy that combines EM-IMO and molecular dynamics with the fine-tuning of parameters permits building backbone models for different conformations of proteins at the near- atomic-resolution. The use of EM-IMO demonstrates that homology modelling and multi-parametric refinement protocols offer a practical strategy for building atomic models based on medium- to high- resolution cryo-EM density maps [125]. Recent developments in single-particle electron cryo-electron microscopy now allow structures to be routinely solved at a resolution close to 3 Å. To facilitate the interpretation of EM reconstructions X-ray packages such as REFMAC have been modified for the optimal fitting of atomic models into EM maps [127]. External

structural information such as interaction between domains and links to their function can also enhance the reliability of the derived atomic models, stabilize refinement and reduce overfitting [116].

Atomic models obtained as a result of flexible fitting should also be evaluated for their correctness and consistency. A Ramachandran plot [128] is routinely used to visualise the distribution of dihedral torsion angles. These angles of a polypeptide backbone are the most dominant local structural parameters that dictate protein folding. Geometrical constraints and steric clashes between atoms of the main chain and sidechains of each residue make some angles disallowed. The assessment of atomic model quality generated using MolProbity [129], and their correlation with the EM density maps with which they are associated need to be provided in publications.

8. Application of the 3D analysis to the T4SS.

Here the focus will be on the analysis of a component of the T4SS structure that will be used as an example of 3D analysis. The structural model of the T4SS was constructed using four electron density maps obtained at resolutions ranging from 2.5 to 6.7 Å [28]. Heterogeneity analysis through classification of 1,300,000 particle images led to a selection of 566,815 particles that were subjected to 3D homogeneous refinement in the absence of symmetry constraints. The largest component of the T4SS that consisted of the IMC-Arches-Stalk complex was first tackled at medium resolution. As a result, the overall structure was obtained at a resolution of 6.18 Å (Figure 13, upper part of the workflow outlined in grey).

From this map two flexible, multi-domain sub-complexes were selected for the further focus refinement involving one of the three “large bulks” of densities (the IMC protomers) located around the central part of the complex, and the central cone shape structure termed the Stalk (Figure 2D). The first task was the analysis of IMC density within the T4SS system based on the identification of a single IMC protomer (shown as a light-yellow oval on the left-hand side of Figure 13). This was achieved by computationally subtracting the remainder of the T4SS (highlighted in blue) from the experimental images resulting in the generation of a 3.7 A map. When computed at lower contour levels (2sigma), substantial density for a further two IMC regions was revealed. A total of five IMC domains were ultimately identified that all appeared to be related by 6-fold symmetry although a sixth subunit was absent.

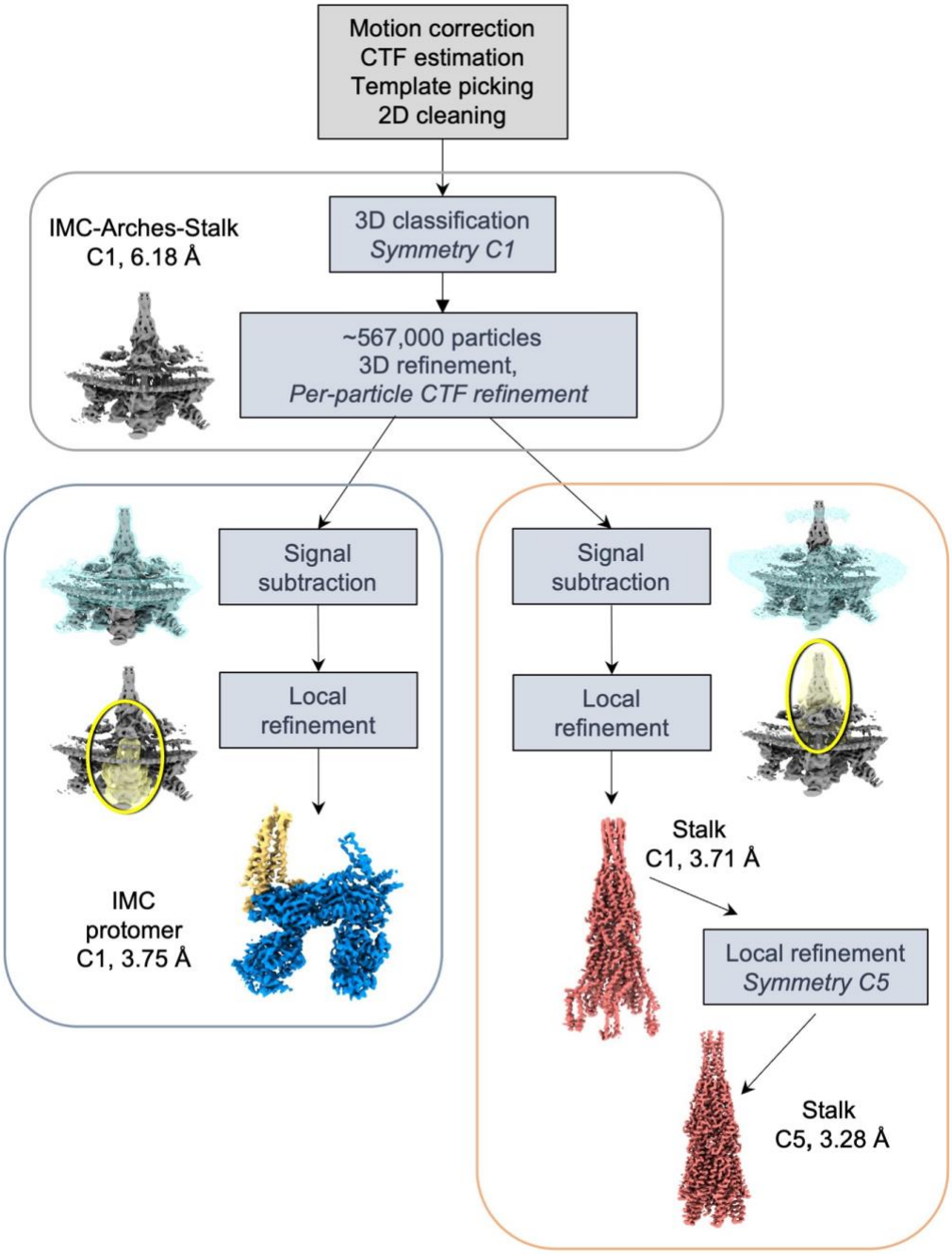

Figure 13. Workflow used to generate the IMC-Arches-Stalk map and the local-refined maps of the single IMC-protomer and Stalk. C1 symmetry was used to obtain a 6.18 Å resolution structure of the complex (EMD-13767). The initial steps used in processing are shown in the grey box. A model was built and used for symmetry analysis of the IMC-Arches, and Stalk. Parts of the structure (outlined with the yellow ovals) were used for refinements after signal subtraction indicated by blue shading. The IMC protomer (EMD-12933) was refined by signal subtraction to 3.75 Å resolution (outlined in the blue box on the left site). The Stalk was refined to 3.71 Å in the absence of symmetry constraints (EMD-12709) and subsequently refined with C5 symmetry to a resolution of 3.28 Å (outlined in reddish-brown on the right of the figure, EMD-12968). The data processing steps (described in the blue rectangles) were done using CryoSPARC, while the grey rectangle indicates processing performed using RELION. [Figure adapted from Ref. 28]

The route for analysis of the Stalk is shown on the right side of Figure 13 **(**outlined in reddish-brown color)**.** Here the Stalk domain is highlighted by a light-yellow oval where the region highlighted in blue within the complex was "subtracted" to enable its analysis. This resulted in a structure at a resolution of 3.71Å. Usage of the 5-fold rotational symmetry aided refinement of the Stalk structure to 3.28 Å. The combination of these refined elements of T4SS and other elements such as the O and I layer of the OMCC provided important information on the structural organization of the complete complex (Figure 2D) [28].

9. Conclusions

Despite the impressive recent achievements within the EM field, there are still many challenges in areas such as the structural studies of large multi-protein complexes with low or no symmetry. Such complexes are typically flexible or can be unstable resulting in a need for better approaches to deal with sample heterogeneity, which invariably means that greater computer power will be required. Cryo-EM and methods of image analysis have become important and powerful tools in the analysis of these forms of bio complexes. Recent advances in the EM field have greatly contributed to unravelling the so far elusive structural and mechanistic details of Gram-negative bacterial secretion systems. This level of details has not only led to a better understanding of the mechanics underling the process of substrate secretion through the T4SS apparatus but has also provided a unique opportunity to visualize how this bacterial nano-machine is structurally organized within both the outer and inner-membranes.

New methods of data and structure classification, remarkable achievements in the prediction of protein atomic models combined with accomplishments in cryo-EM now provide great opportunities for accumulating valuable structural and mechanistic knowledge. These are required for the design and assembly of new bio complexes of medical relevance. Fitting of the predicted models into biologically active EM structures such as previously uncharacterised bacterial complexes will aid in the understanding of host-pathogen interactions and how they can be modulated to curb the spread of pathogenicity and antibiotic resistance.

Acknowledgments:

The authors thank Dr T. Barrett for useful discussions allowing improving the manuscript.

This work was funded by MRC grant MR/K012401/1 to E.V.O. The authors apologize for not complete coverage of all methods owing to space constraints.

References

1. Bartesaghi A, Merk A, Banerjee S et al (2015) 2.2 A resolution cryo-EM structure of beta-galactosidase in complex with a cell-permeant inhibitor. Science 348(6239):1147-1151. doi:10.1126/science.aab1576

2. Herzik MA, Wu M. & Lander GC (2019) High-resolution structure determination of sub-100 kDa complexes using conventional cryo-EM. Nat Commun 10:1032. doi.org/10.1038/s41467-019-08991-8

3. Wu M, Lander GC, Herzik MA (2020) Sub-2 Angstrom resolution structure determination using single-particle cryo-EM at 200 keV. Journal of Structural Biology 4:100020. doi: 10.1016/j.yjsbx.2020.100020

4. Zhang K, Li S, Chiu W. et al (2019) Cryo-EM structure of a 40 kDa SAM-IV riboswitch RNA at 3.7 Å resolution Nat. Commun 10:5511. doi.org/10.1038/s41467-019-13494-7

5. Zhang K, Pintilie GD, Li S, Schmid MF, Chiu W (2020) Resolving individual atoms of protein complex by cryo-electron microscopy. Cell Res 30(12):1136-1139. doi:10.1038/s41422-020-00432-2.

6. Yip KM, Fischer N, Paknia E, Chari A, Stark H (2020) Atomic-resolution protein structure determination by cryo-EM. Nature 587(7832):157-161. doi:10.1038/s41586-020-2833-4.

7. https://www.ebi.ac.uk/emdb/statistics/emdb_resolution_year

8. Barlow M. (2009) What antimicrobial resistance has taught us about horizontal gene transfer. Methods Mol Biol 532:397-411. doi:10.1007/978-1-60327-853-9_23.

9. Costa T, Felisberto-Rodrigues C, Meir A, et al (2015) Secretion systems in Gram-negative bacteria: structural and mechanistic insights. Nat Rev Microbiol 13: 343–359. doi.org/10.1038/nrmicro3456

10. Lyumkis D (2019) Challenges and opportunities in cryo-EM single-particle analysis. J. Biol. Chem 294: 5181-5197. doi:10.1074/jbc.REV118.005602

11. Orlova EV, Saibil HR (2010) Methods for three-dimensional reconstruction of heterogeneous assemblies. Methods in enzymology 482:321-341. doi:10.1016/S0076-6879(10)82013-0

12. Orlova EV, Saibil HR (2011) Structural analysis of macromolecular assemblies by electron microscopy. Chem Rev 111(12):7710-48. doi:10.1021/cr100353t

13. Wu M, Lander GC (2020) Present and Emerging Methodologies in Cryo-EM Single-Particle Analysis. Biophysical Journal 119 (7):1281–1289. doi.org/10.1016/j.bpj.2020.08.027.

14. Baßler J., Hurt E (2019) Eukaryotic Ribosome Assembly. Annual Review of Biochemistry. 88:281-306. doi.org/10.1146/annurev-biochem-013118-110817

15. Watson ZL, Ward FR, Méheust R., et al (2020) Structure of the bacterial ribosome at 2 Å resolution. eLife 9:e60482. doi.org/10.7554/eLife.60482

16. Ludtke SJ (2016) Single-particle refinement and variability analysis in EMAN2.1. Methods Enzymol 579:159-89. doi: 10.1016/bs.mie.2016.05.001

17. Chen M, and Ludtke SJ (2021) Deep learning-based mixed-dimensional Gaussian mixture model for characterizing variability in cryo-EM. Nat. Methods 18(8):930–936. doi:10.1038/s41592-021-01220-5

18. Rabuck-Gibbons JN, Lyumkis D et al (2022) Quantitative mining of compositional heterogeneity in cryo-EM datasets of ribosome assembly intermediates. Structure 30(4):498-509.e4. doi:10.1016/j.str.2021.12.005

19. Zhong ED, Bepler T, Berger B. et al (2021) CryoDRGN: reconstruction of heterogeneous cryo-EM structures using neural networks. Nat Methods 18:176–185. doi.org/10.1038/s41592-020-01049-4

20.Scheres SH (2012) RELION: implementation of a Bayesian approach to cryo-EM structure determination. J. Struct. Biol. 180:519–530. doi:10.1016/j.jsb.2012.09.006.

21.de la Rosa-Trevin JM, Oton J, Marabini R et al (2013) Xmipp 3.0: an improved software suite for image processing in electron microscopy. Journal of structural biology 184(2):321-328. doi:10.1016/j.jsb.2013.09.015

22.Punjani A, Rubinstein J, Fleet D et al (2017) CryoSPARC: algorithms for rapid unsupervised cryo-EM structure determination. Nat Methods 14, 290–296. doi.org/10.1038/nmeth.4169

23. Scheres SH. (2016) Processing of Structurally Heterogeneous Cryo-EM Data in RELION. Methods Enzymol. 579:125-57. doi:10.1016/bs.mie.2016.04.012.

24.Punjani A, Fleet DJ (2021) 3D variability analysis: Resolving continuous flexibility and discrete heterogeneity from single particle cryo-EM. J Struct Biol 213(2):107702. doi:10.1016/j.jsb.2021.107702.

25. Fronzes R, Schafer E, Wang L et al (2009) Structure of a type IV secretion system core complex. Science 323(5911):266-268. doi:10.1126/science.1166101

26. Rivera-Calzada A, Fronzes R, Savva CG et al (2013) Structure of a bacterial type IV secretion core complex at subnanometre resolution. The EMBO journal 32 (8):1195-1204. doi:10.1038/emboj.2013.58

27. Low HH, Gubellini F, Rivera-Calzada A et al (2014) Structure of a type IV secretion system. Nature 508 (7497):550-553. doi:10.1038/nature13081

28. Macé K, Vadakkepat AK, Redzej A et al (2022) Cryo-EM structure of a type IV secretion system. Nature 607(7917):191-196. doi:10.1038/s41586-022-04859-y.

29. Ilangovan A, Connery S, Waksman G (2015) Structural biology of the Gram-negative bacterial conjugation systems. Trends in microbiology 23(5):301-310. doi:10.1016/j.tim.2015.02.012

30. Frank J (2006) Three dimensional electron microscopy of macromolecular assemblies: Visualization of biological molecules in their native state. 2nd edn. Oxford University Press, USA doi.org/10.1093/acprof:oso/9780195182187.001.0001

31. Reimer L (1997) Transmission Electron Microscopy. Springer Series in Optical Sciences, Springer-Verlag, 2nd edn,-New York

32. Spence JCH (2003) High Resolution Microscopy. 3rd edn. OUP Oxford, 2013.

33. Dubochet J, Adrian M, Chang JJ et al (1988) Cryo-electron microscopy of vitrified specimens. Q Rev Biophys 21(2):129-228, doi:10.1017/s0033583500004297

34.Adrian M, Dubochet J, Lepault J et al (1984) Cryo-electron microscopy of viruses. Nature 308 (5954):32-36

35. Lepault J, Dubochet J (1986) Electron microscopy of frozen hydrated specimens: preparation and characteristics. Methods in enzymology 127:719-730. doi.org/10.1016/0076-6879(86)27056-1

36. Vos MR, Bomans PH, Frederik PM et al (2008) The development of a glove-box/Vitrobot combination: air-water interface events visualized by cryo-TEM. Ultramicroscopy 108(11):1478-1483. doi:10.1016/j.ultramic.2008.03.01

37. Jaffe JS, Glaeser RM (1987) Difference Fourier analysis of "surface features" of bacteriorhodopsin using glucose-embedded and frozen-hydrated purple membrane. Ultramicroscopy 23(1):17-28; doi:10.1016/0304-3991(87)90223-3

38. Grassucci RA, Taylor DJ, Frank J (2007) Preparation of macromolecular complexes for cryo-electron microscopy. Nat Protoc 2(12):3239-46. doi:10.1038/nprot.2007.452

39. Ayache J., Beaunier L., Boumendil J et al (2010) Sample Preparation Handbook for Transmission Electron Microscopy. doi:10.1007/978-1-4419-5975-1

40. Cabra V, Samso M (2015) Do's and don'ts of cryo-electron microscopy: a primer on sample preparation and high quality data collection for macromolecular 3D reconstruction. Journal of visualized experiments JoVE(95):52311. doi:10.3791/52311

41. Carragher B, Cheng Y, Frost A et al (2019) Current outcomes when optimizing 'standard' sample preparation for single-particle cryo-EM. J Microsc. Oct;276(1):39-45. doi: 10.1111/jmi.12834.

42. Tivol WF, Briegel A, Jensen GJ (2008) An improved cryogen for plunge freezing. Microscopy and microanalysis of Canada 14 (5):375-379. doi:10.1017/S1431927608080781

43. Faruqi AR, Henderson R (2007) Electronic detectors for electron microscopy. Current opinion in structural biology 17 (5):549-555. doi:10.1016/j.sbi.2007.08.014

44. McMullan G, Chen S, Henderson R et al (2009) Detective quantum efficiency of electron area detectors in electron microscopy. Ultramicroscopy 109(9):1126-1143. doi:10.1016/j.ultramic.2009.04.002

45. Milazzo AC, Moldovan G, Lanman J et al (2010) Characterization of a direct detection device imaging camera for transmission electron microscopy. Ultramicroscopy 110(7):744-747. doi:10.1016/j.ultramic.2010.03.007

46. Levin BDA, (2021) Direct detectors and their applications in electron microscopy for materials science J. Phys. Mater 4 042005. doi:10.1088/2515-7639/ac0ff9

47. Bammes BE, Rochat RH, Jakana J et al (2012) Direct electron detection yields cryo-EM reconstructions at resolutions beyond 3/4 Nyquist frequency. Journal of structural biology 177(3):589-601. doi:10.1016/j.jsb.2012.01.008

48.. Ruskin RS, Yu Z, Grigorieff N (2013) Quantitative characterization of electron detectors for transmission electron microscopy. Journal of structural biology 184(3):385-393. doi:10.1016/j.jsb.2013.10.016

49. Li X, Mooney P, Zheng S, Booth CR et al (2013) Electron counting and beam-induced motion correction enable near-atomic-resolution single-particle cryo-EM. Nature methods 10(6):584-590. doi:10.1038/nmeth.247

50. McMullan G, Faruqi AR, Clare D et al (2014) Comparison of optimal performance at 300keV of three direct electron detectors for use in low dose electron microscopy. Ultramicroscopy 147:156-163. doi:10.1016/j.ultramic.2014.08.002

51. Campbell MG, Cheng A, Brilot AF et al (2012) Movies of ice-embedded particles enhance resolution in electron cryo-microscopy. Structure 20(11):1823-1828. doi:10.1016/j.str.2012.08.026.

52. Abrishami V, Vargas J, Li X, Cheng Y et al (2015) Alignment of direct detection device micrographs using a robust Optical Flow approach. Journal of structural biology 189(3):163-176. doi:10.1016/j.jsb.2015.02.00156.

53 Scheres SHW (2014) Beam-induced motion correction for sub-megadalton cryo-EM particles eLife 3:e03665. doi.org/10.7554/eLife.03665

54. Zheng, S., Palovcak, E., Armache, JP. et al (2017) MotionCor2: anisotropic correction of beam-induced motion for improved cryo-electron microscopy. Nat Methods 14:331–332. doi.org/10.1038/nmeth.4193

55, Zivanov J, Nakane T, Scheres SHW (2019) A Bayesian approach to beam-induced motion correction in cryo-EM single-particle analysis. IUCrJ. 6(Pt 1):5-17. doi:10.1107/S205225251801463X.

56. Glaeser RM (1971) Limitations to significant information in biological electron microscopy as a result of radiation damage. Journal of ultrastructure research 36(3):466-482. doi.org/10.1016/S0022-5320(71)80118-1

57. Taylor KA, Glaeser RM (1976) Electron microscopy of frozen hydrated biological specimens. Journal of ultrastructure research 55(3):448-456. doi.org/10.1016/S0022-5320(76)80099-8

58. Knapek E, Dubochet J (1980) Beam damage to organic material is considerably reduced in cryo-electron microscopy. Journal of molecular biology 141(2):147-161. doi.org/10.1016/0022-2836(80)90382-4

59 Chiu W, Jeng TW (1982) Electron radiation sensitivity of protein crystals. Ultramicroscopy 10 (1-2):63-69. doi.org/10.1016/0304-3991(82)90188-7

60. Chiu W (1986) Electron microscopy of frozen, hydrated biological specimens. Annual review of biophysics and biophysical chemistry 15:237-257. doi:10.1146/annurev.bb.15.060186.001321

61. Burmeister WP (2000) Structural changes in a cryo-cooled protein crystal owing to radiation damage. Acta Crystallogr D Biol Crystallogr 56(Pt 3):328-341. doi:10.1107/s0907444999016261

62. Egerton RF, Li P, Malac M (2004) Radiation damage in the TEM and SEM. Micron 35(6):399-409. doi:10.1016/j.micron.2004.02.003

63. Bartesaghi A, Matthies D, Banerjee S et al (2014) Structure of beta-galactosidase at 3.2-A resolution obtained by cryo-electron microscopy. Proceedings of the National Academy of Sciences of the United States of America 11(32):11709-11714. doi:10.1073/pnas.1402809111

64. Carlson DB, Evans JE (2012) Low-Dose Imaging Techniques for Transmission Electron Microscopy. The Transmission Electron Microscope,. InTech, China, doi: 10.5772/36614

65. Thon F (1966) Zur Defokussierungsabh ä ngigkeit des Phasenkontrastes bei der elektronenmikroskopischen Abbildung. Naturforschg 21a:476 – 478

66. Wade RH. (1992) A brief look at imaging and contrast transfer Ultramicroscopy. 46:145-156. doi.org/10.1016/0304-3991(92)90011-8

67. Rohou A, Grigorieff N (2015) CTFFIND4: Fast and accurate defocus estimation from electron micrographs. Journal of structural biology 192(2):216-221. doi:10.1016/j.jsb.2015.08.00867,

68. Grant T, Rohou A, Grigorieff N et al (2018) cisTEM, user-friendly software for single-particle image processing eLife 7:e35383. doi.org/10.7554/eLife.35383

69. Ludtke SJ (2016) Single-Particle Refinement and Variability Analysis in EMAN2.1. in Methods Enzymol 579:159-189. Elsevier, United States. doi:10.1016/bs.mie.2016.05.001

70. van Heel M, Gowen B, Matadeen R, et al (2000) Single-particle electron cryo-microscopy: towards atomic resolution Q. Rev. Biophys. 33: 307-369. doi:10.1017/S0033583500003644

71. Wagner T, Merino F, Stabrin M et al (2019) SPHIRE-crYOLO is a fast and accurate fully automated particle picker for cryo-EM. Commun Biol 2:218. doi.org/10.1038/s42003-019-0437-z

72. Wiener N (1964) Extrapolation, Interpolation, and Smoothing of Stationary Time Series; Wiley: New York

73. Mancini E J, Fuller SD (2000) Acta Crystallogr., Sect. D: Biol D56:1278-1287. doi.org/10.1107/S0907444900010817

74. Smith JM (1999) Ximdisp--A visualization tool to aid structure determination from electron microscope images. Journal of structural biology 125(2-3):223-228. doi:10.1006/jsbi.1998.4073

75. Scheres SH (2015) Semi-automated selection of cryo-EM particles in RELION-1.3. Journal of structural biology 189(2):114-122. doi:10.1016/j.jsb.2014.11.010

76. Zhang K (2017) Fully automatic accurate, convenient and extremely fast particle picking for EM. https://sbgrid.org/software/titles/gautomatch

77. Langlois R, Pallesen J, Ash JT et al (2014) Automated particle picking for low-contrast macromolecules in cryo-electron microscopy. Journal of structural biology 186(1):1-7. doi:10.1016/j.jsb.2014.03.001

78. Heymann JB, Belnap DM (2007) Bsoft: image processing and molecular modeling for electron microscopy. Journal of structural biology 157(1):3-18. doi:10.1016/j.jsb.2006.06.006

79. Roseman AM (2004) FindEM--a fast, efficient program for automatic selection of particles from electron micrographs. J Struct Biol 145(1-2):91-99

80. Voss NR, Yoshioka CK, Radermacher M et al (2009) DoG Picker and TiltPicker: software tools to facilitate particle selection in single particle electron microscopy. J Struct Biol 166(2):205-13. doi: 10.1016/j.jsb.2009.01.004.

81. Bepler T, Morin A, Rapp M et al (2019). Positive-unlabeled convolutional neural networks for particle picking in cryo-electron micrographs. Nature Methods 16:1153–1160. doi.org/10.1038/s41592-019-0575-8

82. Al-Azzawi A, Ouadou A, Max H et al (2020) DeepCryoPicker: fully automated deep neural network for single protein particle picking in cryo-EM. BMC Bioinformatics 21:509. doi.org/10.1186/s12859-020-03809-7

83 Tegunov D, Cramer P (2019) Real-time cryo-electron microscopy data preprocessing with Warp. Nat Methods. 16(11):1146-1152. doi:10.1038/s41592-019-0580-y

84.Van Heel M, Portugal RV, Schatz M (2009) Multivariate Statistical Analysis in Single Particle (Cryo) Electron Microscopy. An electronic textbook: Electron microscopy in Life Science. 3D-EM Network of Excellence,

85 Sigworth FJ (1998) A maximum-likelihood approach to single-particle image refinement. Journal of structural biology. 122(3):328-339. doi:10.1006/jsbi.1998.4014

86. Sigworth FJ, Doerschuk PC, Carazo JM et al (2010). An introduction to maximum-likelihood methods in cryo-EM. Methods Enzymol. 482:263-94. doi: 10.1016/S0076-6879(10)82011-7.

87 Myung IJ (2003) Tutorial on maximum likelihood estimation. J Math Psyc 47(1):90-100. doi.org/10.1016/S0022-2496(02)00028-7

88 Scheres SH (2010) Classification of structural heterogeneity by maximum-likelihood methods. Methods in enzymology 482:295-320. doi:10.1016/S0076-6879(10)82012-9

89. MacQueen (1967) J. Proceedings of the 5th Berkeley Symposium on Mathematical Statistics and Probability. University of California Press; Berkeley, CA, USA Some methods for classification and analysis of multivariate observations,Volume 1 Statistics: 281–297

90. Hartigan JA and Wong MA (1979) Algorithm AS 136: A K-Means Clustering Algorithm. Journal of the Royal Statistical Society. Series C (Applied Statistics). 28(1):100-108. doi.org/10.2307/2346830

91. Punjani A, Brubaker MA (2015) Microscopic Advances with Large-Scale Learning: Stochastic Optimization for Cryo-EM. https://arxiv.org/pdf/1501.04656.pdf

92. Al-Azzawi A, Ouadou A, Tanner JJ et al (2019) A Super-Clustering Approach for Fully Automated Single Particle Picking in Cryo-EM. Genes (Basel) 10(9):666. doi:10.3390/genes10090666.

93. Chung JM, Durie CL, Lee J (2022) Artificial Intelligence in Cryo-Electron Microscopy. Life, 12:1267. doi.org/10.3390/ life12081267

94. Botifoll M., Pinto-Huguet, Jordi Arbiol J. (2022) Machine learning in electron microscopy for advanced nanocharacterization: current developments, available tools and future outlook. Nanoscale Horiz. **7**:1427-1477, doi:10.1039/D2NH00377E

95. Skalidis I, Kyrilis FL, Tüting C et al (2022) Cryo-EM and artificial intelligence visualize endogenous protein community members. Structure 30(4):575-589.e6. doi: 10.1016/j.str.2022.01.001.

96. Orlov SS (1976) Theory of three dimensional reconstruction - Conditions of a complete set of projections. Sov Phys Crystallogr 20:312-314

97. Crowther RA, DeRosier DJ, Klug A (1970) The Reconstruction of a Three-Dimensional Structure from Projections and its Application to Electron Microscopy. Proceedings of the Royal Society A 317 (1530: 319-340. doi.org/10.1098/rspa.1970.0119

98. Crowther RA (1971) Procedures for three-dimensional reconstruction of spherical viruses by Fourier synthesis from electron micrographs. Philosophical transactions of the Royal Society of London Series B, Biological sciences 261(837):221-230. doi:10.1098/rstb.1971.0054

99. van Heel M, Orlova EV, Harauz G et al (1997) Angular reconstitution in three-dimentional electron microscopy: historical and theoretical aspects. Scanning microscopy 11:195-210

100. Fuller SD (1987) The T=4 envelope of Sindbis virus is organized by interactions with a complementary T=3 capsid. Cell 48(6):923-934.doi:10.1016/0092-8674(87)90701-x

101. De Rosier DJ, Klug A (1968) Reconstruction of three dimensional structures from electron micrographs. Nature 217(5124):130-134. doi.org/10.1038/217130a0

102. Harauz G, van Heel M (1986) Exact filters for general geometry three-dimensional reconstruction. Optik 73:146-156

103. Herman GT (1980) Image Reconstruction from Projections: The Fundamentals of Computerized Tomography. Academic Press, New York. doi.org:10.1002/zamm.19830630227

104. Penczek PA (2010) Fundamentals of three-dimensional reconstruction from projections, vol 482. Methods in Enzymology: Cryo-EM, Part B, 3-D Reconstruction. Academic Press, Elsevier, San Diego, CA. doi:10.1016/S0076-6879(10)82001-4

105. DeRosier DJ, Moore PB (1970) Reconstruction of three-dimensional images from electron micrographs of structures with helical symmetry. Journal of molecular biology 52(2):355-369. doi:org10.1016/0022-2836(70)90036-7

106. Haselbach D, Schrader J, Lambrecht F et al. (2017) Long-range allosteric regulation of the human 26S proteasome by 20S proteasome-targeting cancer drugs. Nat Commun 8:15578. doi.org/10.1038/ncomms15578

107.Haselbach D, Komarov I, Agafonov DE et al (2018). Structure and Conformational Dynamics of Human Spliceosome B act Complex. Cell 172: 454–464. doi:10.1016/j.cell.2018.01.010

108. Glaeser RM, Downing KH, DeRosier DJ et al (2007) Electron Crystallography of Biological Macromolecules. Oxford University Press, New York.

109. van Heel M, Schatz M (2005) Fourier shell correlation threshold criteria. Journal of structural biology 151(3):250-262. doi:10.1016/j.jsb.2005.05.009

110. Rosenthal PB, Henderson R (2003) Optimal determination of particle orientation, absolute hand, and contrast loss in single-particle electron cryomicroscopy. Journal of molecular biology 333(4):721-745. doi:10.1016/j.jmb.2003.07.013

111. Scheres SH, Chen S (2012) Prevention of overfitting in cryo-EM structure determination. Nature methods 9(9):853-854. doi:10.1038/nmeth.2115

112. Chen S, McMullan G, Faruqi AR et al (2013) High-resolution noise substitution to measure overfitting and validate resolution in 3D structure determination by single particle electron cryomicroscopy. Ultramicroscopy 135:24-35. doi:10.1016/j.ultramic.2013.06.004

113. Kucukelbir A, Sigworth FJ, Tagare HD (2014) Quantifying the local resolution of cryo-EM density maps. Nature methods 11(1):63-65. doi:10.1038/nmeth.2727

114. Villa E, Lasker K (2014) Finding the right fit: chiseling structures out of cryo-electron microscopy maps. Current opinion in structural biology 25:118-125. doi:10.1016/j.sbi.2014.04.001

115. Topf M, Lasker K, Webb B et al (2008) Protein structure fitting and refinement guided by cryo-EM density. Structure 16(2):295-307. doi:10.1016/j.str.2007.11.016

116. Brown A, Long F, Nicholls RA et al (2015) Tools for macromolecular model building and refinement into electron cryo-microscopy reconstructions. Acta Crystallogr D Biol Crystallogr 7(Pt 1):136-153. doi:10.1107/S1399004714021683

117. Kelley LA, Mezulis S, Yates CM et al (2015) The Phyre2 web portal for protein modeling, prediction and analysis. Nat Protoc 10(6):845-858. doi:10.1038/nprot.2015.053

118. Yang J, Yan R, Roy A, Xu D et al (2015) The I-TASSER Suite: protein structure and function prediction. Nature methods 12(1):7-8. doi:10.1038/nmeth.3213

119. Baek M, DiMaio F, Anishchenko I et al (2021) Accurate prediction of protein structures and interactions using a three-track neural network. Science 373(6557):871-876. doi: 10.1126/science.abj8754

120. Jumper J, Evans R, Pritzel A et al (2021) Highly accurate protein structure prediction with AlphaFold. Nature 596:583–589. doi.org/10.1038/s41586-021-03819-2

121.Pettersen EF, Goddard TD, Huang CC et al (2004) UCSF Chimera--a visualization system for exploratory research and analysis. Journal of computational chemistry 25(13):1605-1612. doi:10.1002/jcc.20084

122. Emsley P, Cowtan K (2004) Coot: model-building tools for molecular graphics. Acta Crystallogr D Biol Crystallogr 60 (Pt12Pt1):2126-2132. doi:10.1107/s0907444904019158

123 Lopéz-Blanco JR, Chacón P (2013) iMODFIT: efficient and robust flexible fitting based on vibrational analysis in internal coordinates. Journal of Structural Biology 184(2):261-270. doi:10.1016/j.jsb.2013.08.010.

124. Adams PD, Afonine PV, Bunkoczi G et al (2010) PHENIX: a comprehensive Python-based system for macromolecular structure solution. Acta Crystallogr D Biol Crystallogr 66(Pt2):213-221. doi:10.1107/S0907444909052925

125. Kim DE, Chivian D, Baker D (2004) Protein structure prediction and analysis using the Robetta server. Nucleic Acids Res. 32:W526–W531, doi:10.1093/nar/gkh468

126. Zhu J, Cheng L, Fang Q et al (2010) Building and refining protein models within cryo-electron microscopy density maps based on homology modeling and multiscale structure refinement. Journal of molecular biology 397(3):835-851. doi:10.1016/j.jmb.2010.01.041

127. Kovalevskiy O, Nicholls RA, Long F et al (2018) Overview of refinement procedures within REFMAC5: utilizing data from different sources. Acta Crystallogr D Struct Biol 74(Pt 3):215-227. doi: 10.1107/S2059798318000979.

128. Williams CJ, Headd JJ, Moriarty NW et al (2018) MolProbity: More and better reference data for improved all-atom structure validation. Protein Sci 27(1):293-315. doi: 10.1002/pro.3330.

129. Ramachandran GN, Ramakrishnan C, Sasisekharan V (1963) Stereochemistry of polypeptide chain configurations. J Mol Biol 7:95-9. doi: 10.1016/s0022-2836(63)80023-6.